

XMM-Newton survey of two upper Scorpius regions^{★,★★}

C. Argioffi¹, F. Favata², E. Flaccomio³, A. Maggio³, G. Micela³, G. Peres¹, and S. Sciortino³

¹ Dipartimento di Scienze Fisiche ed Astronomiche, Sezione di Astronomia, Università di Palermo, Piazza del Parlamento 1, 90134 Palermo, Italy

e-mail: [argi;peres]@astropa.unipa.it

² Astrophysics Division – Research and Science Support Department of ESA, Postbus 299, 2200 AG Noordwijk, The Netherlands
e-mail: Fabio.Favata@rssd.esa.int

³ INAF – Osservatorio Astronomico di Palermo, Piazza del Parlamento 1, 90134 Palermo, Italy
e-mail: [ettoreff;maggio;giusi;sciorti]@astropa.unipa.it

Received 23 May 2006 / Accepted 11 July 2006

ABSTRACT

Aims. We studied X-ray emission from young stars by analyzing the deep XMM-Newton observations of two regions of the Upper Scorpius association with an age of 5 Myr.

Methods. Based on near infrared and optical photometry we identified 22 Upper Scorpius photometric members among the 224 detected X-ray sources. We derived coronal properties of Upper Scorpius stars by performing X-ray spectral and timing analyses. The study of four strong and isolated stellar flares allowed us to derive the length of the flaring loops.

Results. Among the 22 Upper Scorpius stars, 13 were identified as Upper Scorpius photometric members for the first time. The sample includes 7 weak-line T Tauri stars and 1 classical T Tauri star, while the nature of the remaining sources is unknown. Except for the intermediate mass star HD 142578, all the detected USco sources are low-mass stars of spectral types ranging from G to late M. The X-ray emission spectrum of the most intense Upper Scorpius sources indicates metal depleted plasma with temperature of ~ 10 MK, resembling the typical coronal emission of active main sequence stars. At least 59% of the detected members of the association have variable X-ray emission, and the flaring coronal structures appear shorter than or comparable to the stellar radii already at the Upper Scorpius age. We also found indications of increasing plasma metallicity (up to a factor 20) during strong flares. We identified a new galaxy cluster among the 224 X-ray source detected: the X-ray spectrum of its intra cluster medium indicates a redshift of $\sim 0.41 \pm 0.02$.

Key words. stars: abundances – stars: activity – stars: coronae – stars: flare – stars: pre-main sequence – X-rays: stars

1. Introduction

Pre-main sequence (PMS), low-mass stars at an age of a few Myr are usually classified as classical T Tauri stars (CTTSs) if they still accrete material from their circumstellar disk; they become weak-line T Tauri stars (WTTs) when the accretion ends. This classification is usually based on the $H\alpha$ line (e.g. Hartmann et al. 1994; White & Basri 2003, and references therein).

Strong X-ray radiation is a common characteristic of PMS low-mass stars (e.g. Feigelson & Montmerle 1999, and references therein). The X-ray emission from accreting and non-accreting PMS stars is produced by hot plasma ($T \sim 1-100$ MK), suggesting therefore that coronal activity is present irrespective of the accretion status. However, low-resolution X-ray spectra hinted at significant differences between CTTSs and WTTs. CTTSs reveal lower X-ray luminosity compared to the non-accreting WTTs, and appear to produce harder X-ray

spectra than WTTs (Neuhäuser et al. 1995; Tsujimoto et al. 2002; Flaccomio et al. 2003a; Preibisch et al. 2005; Flaccomio et al. 2006). These results indicate that accretion processes and circumstellar disks do indeed affect the X-ray emission of PMS stars. How this influence occurs is still a debated question. During the CTTS stage, the infalling circumstellar material, heated by the shock with the photosphere to temperatures of a few MK, is a possible source of soft X-ray emission (Kastner et al. 2002), while protostellar jets may also contribute to the X-ray emission of PMS stars (Pravdo et al. 2001; Favata et al. 2002). Long coronal loops found in PMS stars (Favata et al. 2005) suggest that interactions between the magnetosphere and the circumstellar disk may occur and affect the coronal plasma characteristics. On the other hand, the lack of accretion streams and close circumstellar material in WTTs implies that their X-ray radiation may only be produced by magnetically confined coronal plasma.

The different rotational periods of CTTSs and WTTs, shown by Bouvier et al. (1993), may explain the differences in the X-ray properties, as happens for main sequence stars (Pallavicini et al. 1981; Pizzolato et al. 2003). However, several studies suggested that the X-ray luminosity vs. rotational period relationship is not as clear for PMS stars as in the case of MS stars, possibly because most of the PMS stars appear to be in

* Appendix A, Tables 1, 2 and Figs. 6, 7 are only available in electronic form at <http://www.aanda.org>

** Tables B.1, C.1, and D.1 are only available in electronic form at the CDS via anonymous ftp to [cdsarc.u-strasbg.fr](ftp://cdsarc.u-strasbg.fr) (130.79.128.5) or via <http://cdsweb.u-strasbg.fr/cgi-bin/qcat?J/A+A/459/199>

the saturated or supersaturated regime or because other parameters, like stellar age, may alter the X-ray activity level (Stelzer & Neuhäuser 2001; Flaccomio et al. 2003b; Stassun et al. 2004; Preibisch & Feigelson 2005; Preibisch et al. 2005).

Analyzing X-ray emission from WTTs, where the lack of close circumstellar material limits corona-disk interactions and excludes accretion driven X-ray emission, can provide insightful results for comprehending coronal emission from young stars. These findings may also be useful for understanding the properties of coronal plasma of CTTs. To this aim we analyzed two *XMM-Newton* observations of two fields in the Upper Scorpius association, the younger portion of the Scorpius Centaurus OB association.

The Scorpius Centaurus OB association is one of the closest regions of recent star formation. It contains an estimated population of ~ 5000 – $10\,000$ stars with masses higher than $0.1 M_{\odot}$ (de Geus 1992). It is the result of a star formation process started ~ 15 Myr ago in a giant molecular cloud. The Scorpius Centaurus OB association is composed of three subgroups: the Upper Scorpius (USco), the Upper Centaurus Lupus (UCL), and the Lower Centaurus Crux (LCC). These three subgroups have different ages (ranging from 5 to 15 Myr) suggesting that star formation proceeded progressively in different parts of the original molecular cloud. According to the proposed scenario, the older OB stars, located in the UCL subgroup, produced shock fronts in the original giant molecular cloud by their strong winds and subsequent supernova explosions, and hence triggered new star formations (de Geus 1992). These shock waves passed ~ 5 Myr ago in the USco region thereby activating the USco star formation. Once the most massive USco stars evolved, ~ 1.5 Myr ago, their supernova explosions dissolved the interstellar material in the USco region, thereby stopping the star formation process; therefore, the USco region appears free of dense interstellar material. Moreover, the shocks produced by massive USco stars induced the latest stage of the star formation process in the ρ Ophiuchi cloud, at the margin of the Scorpius Centaurus OB association.

Among the three subgroups of the Scorpius Centaurus OB association, the USco is the youngest. Its age, estimated from high, intermediate, and low-mass stars, is ~ 5 Myr (de Geus et al. 1989; Preibisch et al. 2002; Slesnick et al. 2006). Measured parallaxes of USco members suggest an average distance of ~ 145 pc (de Bruijne et al. 1997), with a scatter of ± 20 pc. The USco region displays a CTTs vs. WTTs ratio of ~ 2 – 5% (Walter et al. 1994; Martin 1998), which is lower than the ratio observed in T associations of a similar age. The supernova shock fronts, which propagated in the USco region ~ 1.5 Myr ago, might have cleaned the local medium and accelerated the dissipation of circumstellar disks of accreting stars (Walter et al. 1994). The vicinity of the USco region and its low circumstellar extinction ($A_V \lesssim 2$ mag, de Geus et al. 1989) offer the opportunity to perform detailed studies of the X-ray emission of T Tauri stars and, in particular, of WTTs, abundant in this region.

In this paper we present the analysis of the *XMM-Newton* observations of two fields of the USco region. In order to select probable PMS candidates of USco we used near infrared (NIR) data of 2MASS and DENIS catalogs. We stress that the 2MASS catalog, thanks to its sky coverage and limiting magnitude, permits complete detection of USco sources down to $\sim 0.02 M_{\odot}$. Moreover we also took advantage of optical photometry (Flaccomio et al. 2000) obtained with two instruments: the Curtis Schmidt (CTIO) telescope and the Danish 1.54 m (ESO) telescope with the Danish Faint Object Spectrograph and Camera.

2. Observations and data analysis

In this section we describe the X-ray and optical observations and the preliminary analyses of the data.

2.1. X-ray observations

XMM-Newton observed two regions of the USco association on August 24 and 26, 2000, with exposures of ~ 53 and ~ 43 ks. For both the observations and for all the EPIC instruments, the medium filters were used to prevent optical contamination in the softer part of the spectra. The log of the *XMM-Newton* observations is reported in Table 1.

We processed both observations using the SAS.V6.0 standard tasks *epchain* and *emchain*. We selected events with energy ranging from 0.3 to 7.9 keV: below 0.3 keV the instruments response is not well-calibrated, above 7.9 keV the background dominates the stellar X-ray emission.

To maximize the S/N we performed time screening of the X-ray data discarding time intervals affected by high background count rates. The screened good time intervals correspond to 85–95% of the initial exposures, while the background count rate of the EPIC/PN instrument is reduced by a factor ~ 2 .

2.2. Optical photometric observations

The photometric observations were performed with the CTIO Curtis-Schmidt and Danish 1.54 m telescopes. The observed fields of view for each instrument and the relevant bands are reported in Table 2. Note that the fields of view do not entirely cover the two *XMM-Newton* observations (see Sect. 3). Data reduction was carried out using IRAF tools. We performed aperture photometry on all fields and transformed the instrumental magnitude to the standard Johnson-Cousin system through the use of the Landolt (1992) standard catalog.

For each field we performed either two or three distinct observations with the same filter. In order to estimate the uncertainties of our photometry as a function of star brightness we calculated, for each star, the dispersion of the magnitudes independently measured and took the average. These uncertainties are consistent with those formally derived by combining the statistical errors on the instrumental magnitudes and the uncertainties on the transformations between instrumental magnitudes to the standard system.

We considered only objects with (mean) uncertainties on V , I , and $V - I$ less than ~ 0.1 mag. This translates into the limiting magnitudes: $V \leq 19.0$ for the Danish 1.54 m, $V \leq 16.5$ for the Curtis Schmidt, the sources detected and their photometry are listed in Tables B.1 and C.1¹.

2.3. X-ray source detection

We searched for X-ray sources in the two observations by applying the wavelet transform detection algorithm developed for *ROSAT* data (Damiani et al. 1997a,b) and adapted to the EPIC case (Pillitteri et al. 2006). We performed X-ray source detection on composite count rate images obtained by the

¹ Tables B.1 and C.1 are available at the CDS. Table B.1 contains the following information: Column 1 lists the identification number of the source, Cols. 2 and 3 the source position, Cols. 4–8 the V , $B - V$, $U - B$, $V - R$, and $V - I$ values. Table C.1 contains the following information: Col. 1 lists the identification number of the source, Cols. 2 and 3 the source position, Cols. 4–6 the V , $V - R$, and $V - I$ values.

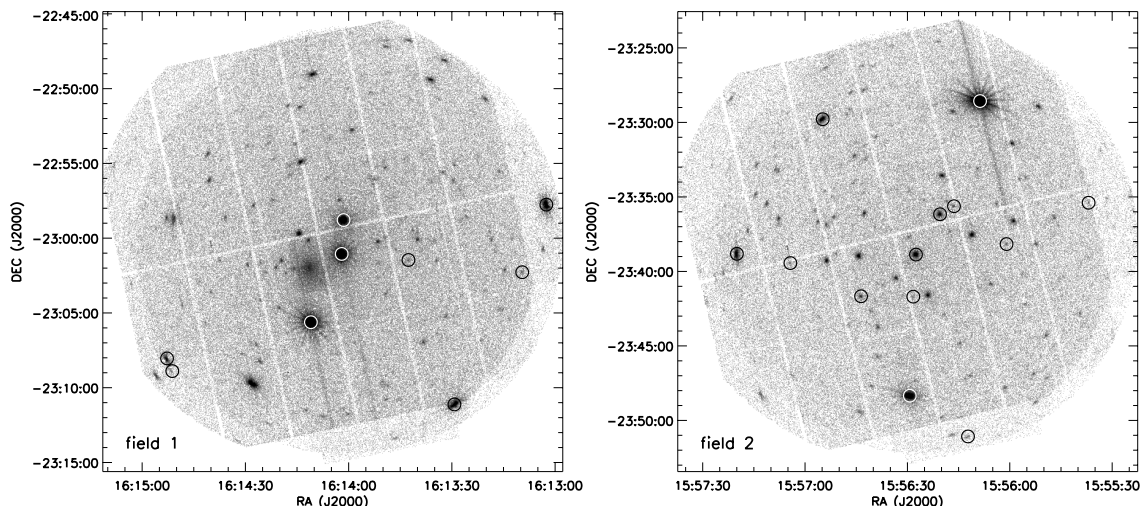


Fig. 1. Composite images (PN+MOS1+MOS2) of the two *XMM-Newton* observations. Circles mark X-ray sources selected as photometric USco members.

superposition of the three EPIC instruments, shown in Fig. 1. We established significance thresholds of 4.8 and 4.9σ for fields 1 and 2, respectively, in order to obtain on average one spurious source per field due to background fluctuations². Spurious detections due to peculiar point spread function features or to out-of-time event signatures are, however, present but are easily recognized by inspection and discarded. We also removed spurious sources due to hot pixels from the list. We obtained 117 and 107 sources in fields 1 and 2, respectively. The list of the detected *XMM-Newton* sources is reported in Table D.1³.

2.4. Extraction of X-ray data

For each detected source, we extracted events from a circle centered on the source position. The extraction radii vary from source to source in order to maximize the S/N ratio and to avoid inclusion of other nearby sources. They range from $10''$ for sources very close to each other to $60''$ for intense and isolated sources. Background events were extracted from annular regions centered on the source or from a circular region located near the source (when possible at the same off-axis and on the same CCD); usually the background region was chosen to be larger than the source extraction region. For each source, an ancillary response function and a redistribution matrix function were computed using SAS tasks. Source spectra were rebinned to obtain at least 20 counts per bin. We verified that EPIC data were in all cases not affected by significant pile-up. Analysis was performed considering single, double, triple, or quadruple pixel events ($PATTERN \leq 12$), except for PN spectral analysis, where only single or double pixel events ($PATTERN \leq 4$) were retained.

² The threshold levels were determined by applying the following procedure: we simulated empty fields characterized by the same background levels of the two USco *XMM-Newton* observations; we performed source detections with different threshold levels; we estimated the threshold that provides the requested number of spurious sources. The derived threshold depends on the background levels, so we adopted different threshold levels for the two observations.

³ Table D.1, available at the CDS, contains the following information: Col. 1 lists the identification number of the X-ray source, Cols. 2 and 3 the source position, Col. 4 the PN count rate, Cols. 5 and 6 the X-ray colors, Cols. 7–10 the 2MASS and DENIS counterparts.

3. Identifications

We compared our source list with the X-ray sources detected by Sciortino et al. (1998) in a *ROSAT* observation that includes field 2. We detected all the *ROSAT* sources that fall in the *XMM-Newton* field of view with an offset that is always smaller than $6''$, except for the USco 21 *ROSAT* source, which is located $20''$ from the *XMM-Newton* counterpart (source 1 in Table D.1). However, this offset is compatible with the position uncertainty of the *ROSAT* PSPC point-spread function.

We searched for NIR counterparts to the X-ray sources in the 2MASS and in the DENIS catalogs. We also searched for optical counterparts in the photometric CTIO and Danish 1.54 m observations. All these catalogs and observations surveyed different sky areas, and only the 2MASS catalog covers the two *XMM-Newton* fields entirely. Figure 2 shows the *XMM-Newton* fields, together with the area covered by the DENIS, CTIO, and Danish 1.54 m surveys.

Before assigning counterparts to the detected X-ray sources, we used the 2MASS catalog to check the astrometric accuracy of the *XMM-Newton* observations. We measured a systematic and significant offset of $1.5''$ along RA for both observations, by comparing the position of X-ray and 2MASS sources. Hence we corrected X-ray source positions to fix this offset. The astrometry of the CTIO and Danish 1.54 m observations was also registered on the 2MASS coordinate system.

We adopted an identification radius between X-ray and optical/NIR sources of $5''$, estimated from the position offset histograms. This value is comparable to the FWHM of the point-spread function of EPIC instruments.

Searching in the 2MASS point source catalog we found counterparts for 60 X-ray sources, listed in Table D.1. Only for source 1 we did find two counterparts within $5''$. We evaluated the expected numbers of spurious identifications under the assumptions of uncorrelated X-ray and optical/NIR source positions and uniform source distribution over the inspected sky area⁴. We found that up to 6.5 and 9.5 identifications with 2MASS sources may be spurious for fields 1 and 2, respectively.

Only 71% and 78% of the two *XMM-Newton* fields are covered by the DENIS catalog (see Fig. 2). We assigned DENIS counterparts to 53 X-ray sources (out of 170), indicated

⁴ Hence the derived estimates are upper limits.

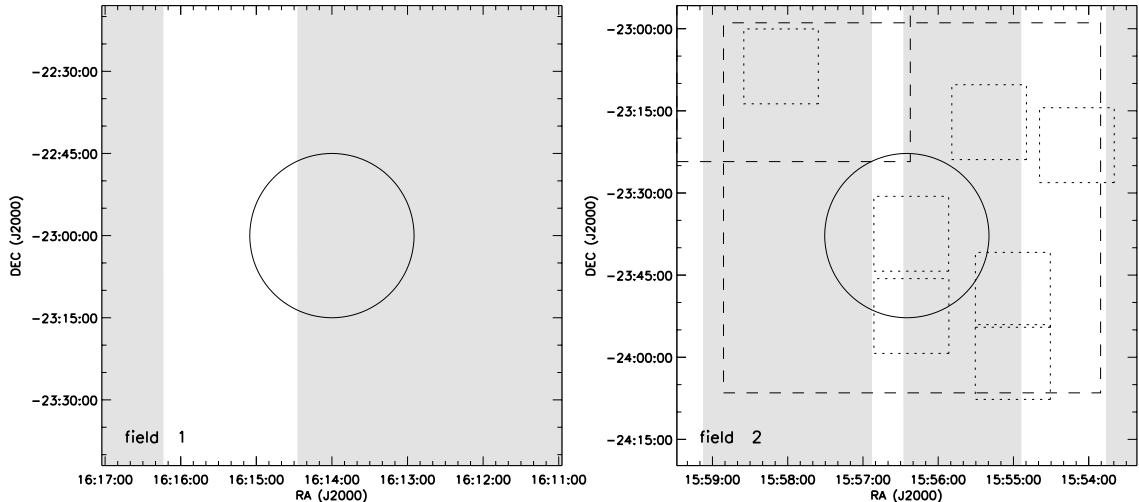


Fig. 2. Schematic maps of the different photometric surveys coverage of the two observed USco fields. Circles indicate the *XMM-Newton* field of view; gray identifies the area covered by the DENIS catalog; dashed squares mark the CTIO observations; short-dashed squares mark the Danish 1.54 m fields.

in Table D.1, and we found 2 counterparts only for source 171. We expect up to 12 and 6.7 spurious identifications for fields 1 and 2, respectively. Among the optical sources detected in the CTIO observations (which surveyed the field 2) we found counterparts for 11 X-ray sources (out of 107), with up to 1.6 spurious identifications. The Danish 1.54 m observations cover 39% of the *XMM-Newton* field 2. We identified Danish counterparts for 13 X-ray sources (out of 54), with up to 3.2 expected spurious identifications. Note that among Danish 1.54 m sources we found two possible counterparts for source 1, whose position coincides with the two 2MASS counterparts. In total we found NIR or optical counterparts for 67 X-ray sources.

3.1. Members of Upper Scorpius

In order to establish which X-ray sources are likely USco members we inspected the color magnitude diagrams (CMD) of the counterparts, displayed in Fig. 3. The USco association covers on the sky an area of ~ 150 deg², with a projected diameter of ~ 14 deg, which corresponds to ~ 35 pc at the distance of the association (Preibisch et al. 2002). Assuming a spherical distribution, the distance spread of USco members in the radial direction should also be ~ 35 pc.

We selected as photometric USco members sources whose photometry is compatible with the values predicted by Siess et al. (2000) or Baraffe et al. (1998). We identified 22 photometric USco members among the 224 detected X-ray sources; photometric members are marked by diamonds in each CMD. All the X-ray sources identified as photometric USco members are detected in the 2MASS survey. Note that the 2MASS catalog contains much fainter objects than the low-mass stars and brown dwarfs of the USco association, as suggested from upper left panel of Fig. 3.

Members are listed in Table 3 together with NIR and optical photometry and available SIMBAD counterparts; they are also marked in Fig. 1. As indicated in Table 3 only 9 of the 22 selected stars were already known USco members. In some uncertain cases, like the two X-ray sources 39 and 70 whose DENIS photometry is located significantly below both the isochrones (upper right panel of Fig. 3), we decided on the basis of the

2MASS data. However, we labeled these sources as uncertain USco members in Table 3.

As mentioned above, X-ray source 1 is associated with two counterparts, located at 1.5 and 4'', detected in both the 2MASS and Danish 1.54 m surveys: the first is the source 2MASS J15561238–2351030 (#1193 in Table C.1) and the second is the source 2MASS J15561210–2351065 (#1189 in Table C.1). In both surveys the magnitudes of the former counterpart are compatible with USco membership (see Table 3). For the latter counterpart the 2MASS photometry is $J = 16.04$, $H = 15.20$, and $K > 13.09$, which suggests it is a background object, while its magnitudes derived from the Danish 1.54 m observation are likely contaminated by the former counterpart. Since X-ray emission is more plausible from a young and nearby star than from a background object, and because the offset is smaller, we assumed that the counterpart of the X-ray source 1 is the source 2MASS J15561238–2351030, which we selected as photometric USco member.

The class of the detected X-ray USco sources ranges from G to late M. The only early star is the counterpart of the X-ray source 100. The set of selected photometric members also contains a known brown dwarf (X-ray source 45). The fields under investigation contain four other known USco members, which were not detected in the X-ray observations: UScoCTIO 92, UScoCTIO 104, UScoCTIO 137, and 2MASS J16131211–2305031 (Ardila et al. 2000; Slesnick et al. 2006), the last three are brown dwarfs (Ardila et al. 2000; Jayawardhana et al. 2003; Slesnick et al. 2006). We list them in the lower part of Table 3 indicating the upper limits to their X-ray emission. Considering the vicinity of the USco association (145 pc) and the low extinction, it is likely that none of the X-ray sources without optical/NIR counterparts is an USco member.

3.2. Comments on individual USco members

Source 1 is located 20'' away from the X-ray source RX J155611.1–235054 (USco 21) detected in a *ROSAT* observation by Sciortino et al. (1998). Given the uncertainty on *ROSAT* positions, the two sources probably coincide, and therefore we assume they are the same source.

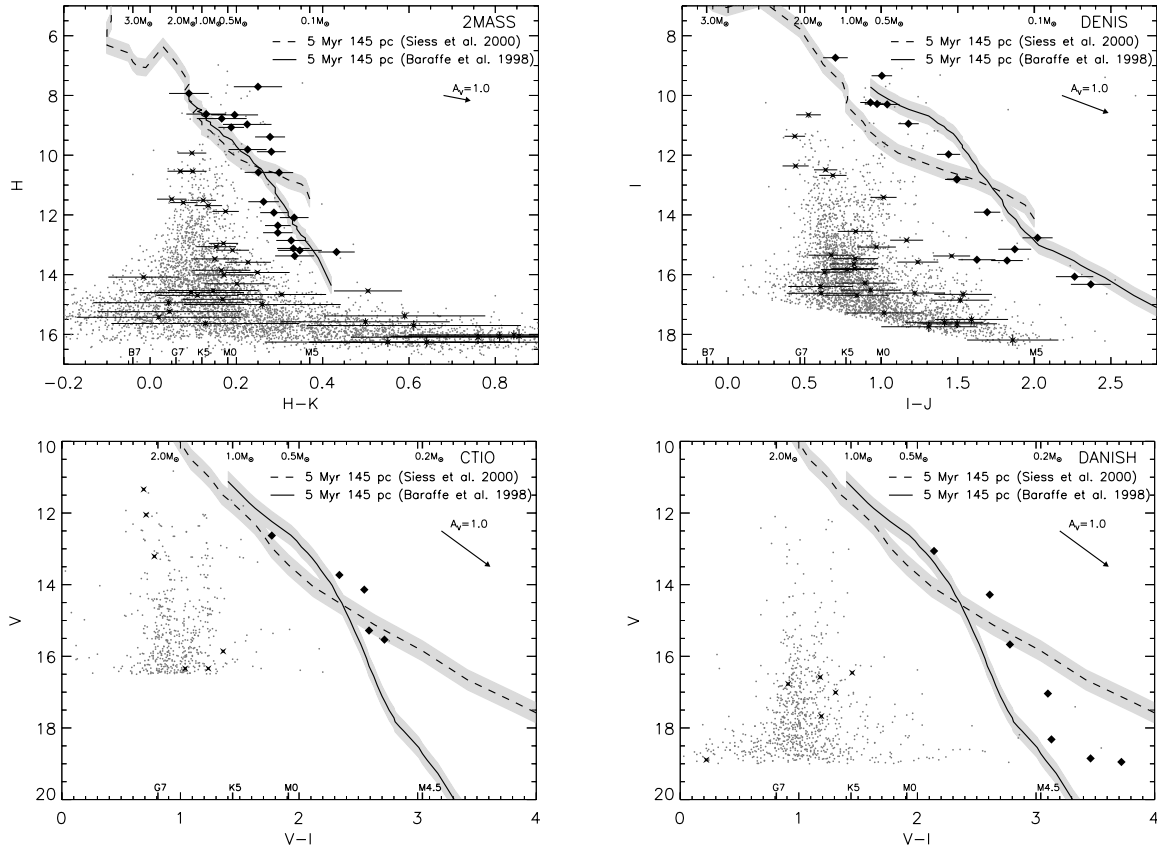


Fig. 3. Color magnitude diagrams of the 2MASS, DENIS, CTIO, and Danish 1.54 m sources that fall in the two *XMM-Newton* fields. In all the plots filled diamonds indicate optical/NIR sources, with X-ray counterparts, selected as photometric USco members. Crosses mark optical/NIR sources, with X-ray counterparts, which are probable background objects. The two isochrones, plotted with dashed and solid lines, are from Siess et al. (2000) and Baraffe et al. (1998), respectively. They correspond to an age of 5 Myr and are scaled to the distance of 145 pc. The Siess et al. model ranges from 0.1 to 7.0 M_{\odot} , while the Baraffe et al. one spans the 0.02–1.4 M_{\odot} interval. The light gray area identifies the locus obtained by varying the distance of ± 20 pc. Masses and spectral types reported in the upper and lower parts of the plot refer to the Siess et al. isochrone.

Source 7 (USco 27, ScoPMS 13) is an M1.5 WTTS, which is a binary system with the two companions separated by $0''.09$ (Köhler et al. 2000). Its young age was shown by Walter et al. (1994) and Martin (1998), who measured the $H\alpha$ emission and high Li abundance. Adams et al. (1998) derived a rotation period of 2.5 ± 0.3 d indicating that this star is a rapid rotator with a period compatible with the average rotation period of WTTSs.

The spectroscopy of source 43 (USco 34, ScoPMS 15) revealed a high lithium abundance and $H\alpha$ emission that together place this source among the WTTSs belonging to the USco association (Walter et al. 1994; Martin 1998). Source 43, whose spectral type is M0, displays a rotational period of 6.2 ± 0.4 d (Adams et al. 1998), which, when combined with the $v \sin i$ measure of 18 km s^{-1} and the predicted radius of $2 R_{\odot}$, indicates an inclination angle *i* of ~ 90 deg.

Source 45 (UScoCTIO 113, DENIS-P J155601.0-233808) was assigned to the USco association by Ardila et al. (2000), who selected it for its photometric properties. Martín et al. (2004) performed optical spectroscopy measuring an $H\alpha$ in emission with an equivalent width of -20 \AA and deriving a spectral type of M6.5. These findings suggest this source is a non-accreting brown dwarf. Its X-ray emission was already reported by Bouy (2004) based on the same *XMM-Newton* observation we present in this work.

Walter et al. (1994) showed that source 95 (USco 21, ScoPMS 14) is an M3 WTTS whose photometry is compatible

with USco membership. Its rotation period of 2.2 d was measured by Adams et al. (1998).

We identified source 100 with the intermediate mass star HD 142578, whose spectral type listed in the SIMBAD database is A2. Photometric measures were conducted by Slawson et al. (1992). Since neither coronal nor wind X-ray emission is expected from this type of star, it is possible that the X-ray radiation is due to an unseen low-mass companion (see Stelzer et al. 2005, and references therein).

Source 114, 158, and 180 are WTTSs of spectral type K1, G4, and K4, respectively, and they show large Li abundance and weak $H\alpha$ emission (Preibisch et al. 1998).

Preibisch et al. (1998) identified source 132 (GSC 06793-00819) as a K0 USco member. They performed optical spectroscopy of this star and measured high Li abundance and $H\alpha$ line in absorption with $EW = 0.96 \text{ \AA}$. Asymmetric features in the $H\alpha$ were observed by Mamajek et al. (2004) who also registered an excess in the *N*-band. From these findings Mamajek et al. propose that this star is actively accreting from its circumstellar disk.

3.3. Extragalactic X-ray sources

We detected 224 sources in the two *XMM-Newton* observations ($\sim 0.4 \text{ deg}^2$), and only 22 were selected as photometric USco members.

Table 3. Probable members of Upper Scorpius.

Source	Name	2MASS			DENIS			CTIO			DANISH			$\log f_X$ ($\text{erg s}^{-1} \text{cm}^{-2}$)	$\log L_X^a$ (erg s^{-1})	Memb ^b		
		J	H	K	K	I	J	K	U	B	V	R	I				R	V
1	RX J155611.1-235054	12.19	11.56	11.30	13.91	12.22	11.24	17.04	15.62	13.94	-13.27 ^c	29.13 ^c	Yes
7	V* V1144 Sco	9.66	8.97	8.74	15.55	14.43	13.73	11.94	11.39	13.06	12.01	10.92	-12.05 ^d	30.36 ^d	W94
31		13.47	12.85	12.53	18.85	17.30	15.39	-14.33 ^c	28.07 ^c	Yes
32		12.98	12.36	12.06	18.95	17.37	15.23	-13.67 ^d	28.73 ^d	Yes
39		13.82	13.19	12.84	15.53	13.71	12.86	-13.93 ^c	28.47 ^c	?
42	RX J155627.5-233848	10.09	9.39	9.11	17.32	15.73	14.14	12.99	11.59	14.28	13.04	11.67	-12.90 ^d	29.50 ^d	Yes
43	V* V1146 Sco	9.73	9.07	8.88	10.95	9.77	8.85	15.18	14.00	12.63	11.78	10.86	-12.59 ^d	29.81 ^d	W94
45	DENIS-P J155601.0-233808	13.86	13.24	12.81	16.33	13.96	12.85	-14.30 ^c	28.11 ^c	A00
62	RX J155620.6-233606	11.26	10.57	10.32	12.81	11.32	10.26	17.83	17.27	15.50	14.33	12.82	15.67	14.37	12.89	-13.31 ^d	29.10 ^d	Yes
66		13.26	12.60	12.30	15.15	13.28	12.21	18.32	16.94	15.19	-13.96 ^c	28.45 ^c	Yes
70		13.93	13.37	13.04	15.50	13.88	13.00	-14.26 ^c	28.14 ^c	?
95	V* V1145 Sco	11.22	10.58	10.28	12.80	11.31	10.33	17.65	16.73	15.28	14.16	12.69	-12.66 ^d	29.75 ^d	W94
100	HD 142578	8.05	7.93	7.84	8.74	8.04	7.87	-11.07 ^d	31.33 ^d	S92
114	GSC 06793-00569	9.32	8.62	8.49	10.28	9.31	8.43	-12.07 ^d	30.33 ^d	P98
123		12.54	11.92	11.64	-13.95 ^c	28.46 ^c	Yes
125		10.57	9.88	9.60	-12.51 ^d	29.90 ^d	Yes
132	GSC 06793-00819	8.28	7.71	7.46	9.34	8.34	7.56	-11.58 ^d	30.83 ^d	P98
144		12.71	12.09	11.76	14.77	12.74	11.76	-13.99 ^c	28.41 ^c	Yes
156		13.76	13.12	12.79	16.07	13.80	12.85	-14.19 ^c	28.22 ^c	Yes
158	GSC 06793-00994	9.38	8.77	8.61	10.24	9.31	8.56	-11.88 ^d	30.52 ^d	P98
173		10.60	9.81	9.59	11.97	10.53	9.49	-12.23 ^d	30.17 ^d	Yes
180	GSC 06793-00797	9.32	8.65	8.45	10.30	9.26	8.38	-11.78 ^d	30.63 ^d	P98
	UScoCTIO 92	13.49	12.90	12.54	15.48	13.52	12.49	<-14.21 ^c	<28.19 ^c	A00
	UScoCTIO 104	13.48	12.86	12.59	15.70	13.47	12.53	<-14.18 ^c	<28.22 ^c	A00
	UScoCTIO 137	15.66	15.00	14.42	<-14.31 ^c	<28.09 ^c	A00
	2MASS J16131211-2305031	14.05	13.45	13.01	16.64	14.17	13.03	<-14.34 ^c	<28.06 ^c	S06

^a X-ray luminosities were evaluated assuming a distance of 145 pc.

^b Question mark indicates stars whose photometry casts some doubt on their membership in Upper Scorpius. W94, A00, S92, P98, S06 designate stars that were identified as Upper Scorpius members by Walter et al. (1994), Ardila et al. (2000), Slawson et al. (1992), Preibisch et al. (1998), and Stesnick et al. (2006) respectively.

^c Unabsorbed X-ray fluxes and luminosities in the 0.5–8.0 keV band were computed starting from PN equivalent count rates and adopting a multiplicative factor of $2.37 \times 10^{-12} \text{ erg cm}^{-2}$.

^d Unabsorbed X-ray fluxes and luminosities in the 0.5–8.0 keV band were evaluated from the best-fit model of the observed spectrum.

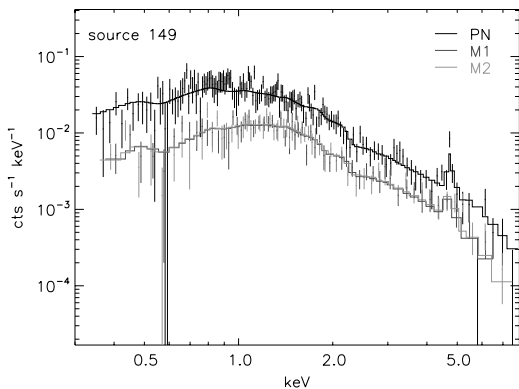


Fig. 4. Observed and best-fit EPIC spectra of the intra cluster medium in the newly discovered galaxy cluster (source 149).

The on-axis detection limits for extragalactic X-ray sources are 3.0 and 3.3×10^{-15} erg s $^{-1}$ cm $^{-2}$ for fields 1 and 2, assuming a power law spectrum with index 1.6. The sensitivity, however, decreases significantly for increasing off-axis angles. Considering the extragalactic X-ray population in the 0.5–8.0 keV band (Alexander et al. 2003), the expected number of extragalactic X-ray sources in the two analyzed *XMM/Newton* observations is ~ 103 and ~ 95 . Hence, only very few X-ray galactic sources, other than the USco members, should be present in the inspected sky areas.

Source 149, near the telescope axis in the *XMM-Newton* field 1 observation (see Fig. 1), shows an extended X-ray emission, that resembles the typical X-ray emission of the intra cluster medium of a galaxy cluster (e.g. Rosati et al. 2002, and references therein). No bibliographic information is available for this source. We fitted its EPIC spectra, extracted within $60''$ from the source position, adopting an absorbed optically-thin isothermal plasma as the model (see Fig. 4). The best-fit model indicates a redshift of 0.41 ± 0.02 (evident from the displacement of the Fe XXV line from 6.7 to 4.7 keV), while the best-fit temperature is 60 ± 10 MK, and the metallicity is 0.4 ± 0.2 with respect to the solar photospheric value.

4. Spectral analysis

In this section we report the X-ray spectral analysis of photometric USco members performed without distinguishing between flaring and quiescent emission. Therefore our analysis represents a study of the time-averaged properties of PMS X-ray emission on time scales of ~ 40 – 50 ks. The spectral analysis was performed using XSPEC V11.3.0 and adopting the Astrophysical Plasma Emission Database (APED V1.3, Smith et al. 2001), based on the ionization equilibrium from Mazzotta et al. (1998).

4.1. X-ray colors

To distinguish the different classes of detected X-ray sources we computed two X-ray colors. We divided the EPIC energy band into three ranges: soft 0.3–0.85, medium 0.85–1.4, and hard 1.4–7.9 keV. For each X-ray source we evaluated the background subtracted number of photons in the three bands, indicating them with S , M , and H . Then we computed the X-ray colors as $XC1 = 2.5 \log(M/S)$ and $XC2 = 2.5 \log(H/M)$, which are listed in Table D.1.

In Fig. 5 we show the observed X-ray colors for the strongest PN sources. We compared the observed values with predictions

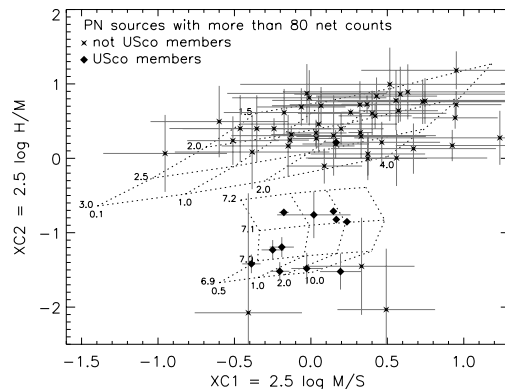


Fig. 5. X-ray colors of PN sources with more than 80 background subtracted counts. S , M , and H indicate the number of net counts in the soft (0.3–0.85 keV), medium (0.85–1.4 keV), and hard (1.4–7.9 keV) energy bands. The upper grid refers to the power law spectra with indices ranging between 1.5 and 3.0 (indicated in the left part of the grid), and hydrogen column density ranging between 0.1 and 4×10^{21} cm $^{-2}$ (indicated in the lower part of the grid). The lower grid corresponds to optically-thin plasma with two thermal components: the lower temperature is kept constant at $\log T_C(\text{K}) = 6.4$, and the higher temperature ranges between $\log T_H(\text{K}) = 6.9$ and 7.2 (indicated on the left part of the grid); the emission measure ratio between the two components EM_H/EM_C varies from 0.5 to 10 (indicated in the lower part of the grid); the hydrogen column density and the metallicity are 1.5×10^{21} cm $^{-2}$ and 0.15 Fe_\odot , respectively (these values were derived from the X-ray spectral analysis of the X-ray brightest USco sources, see Sect. 4.2).

based on two types of models: power law spectra and optically-thin collisionally-excited plasma, represented in Fig. 5 by the upper and lower dotted grids.

All the USco members have $XC1$ and $XC2$ colors that are very compatible with the expected values for coronal sources. The only USco member in this plot that falls in the upper grid is source 100, the intermediate mass star HD 142578, which has $XC2 = 0.20 \pm 0.01$. This source is characterized by a large flare (see Sect. 5.2.3) during which the count rate increases by a factor ~ 100 and the plasma temperature reaches $T \sim 70$ MK. However the $XC2$ color of its quiet phase is -1.14 ± 0.18 , hence compatible with the other USco members.

The observed $XC2$ values have bimodal distribution separated by the distinguishing value $XC2 \approx -0.5$. USco members, all but source 100, have $XC2 < -0.5$. Three other X-ray sources (sources 182, 200, and 209), display $XC2$ colors compatible with, or even softer than, that of the USco members. These three sources have 2MASS counterparts, and their X-ray colors suggest they are background stars. On the other hand, most non USco members in Fig. 5 show positive $XC2$ values. Only 20% of these X-ray sources have 2MASS counterparts, compatible with most of them being extragalactic sources with harder spectra.

The $XC1$ color is very sensitive to the column density value. A change in the N_H produces a variation in the $XC1$ colors that is twice the corresponding variation of $XC2$. In particular, a change of a factor 2 for N_H causes an increase $XC1$ of ~ 0.4 . Since the predicted grids, evaluated for typical coronal temperatures, describe the observed X-ray colors of selected USco members well, we are confident that the adopted N_H is reliable.

4.2. Spectral fitting

We analyzed the X-ray spectra of all the sources identified as photometric members of the USco association with more

than 200 total PN counts. We also analyzed the spectra of the two USco stars (source 114 and 180) that fall outside the PN detector but with high S/N MOS spectra. With these criteria we selected a subset of 13 sources among the 22 photometric members. We performed simultaneous spectral fitting of PN, MOS1 and MOS2 data, except for the faintest sources where only the PN spectrum was studied. Finally, for source 132 we did not consider MOS1 data since they were not compatible with the PN and MOS2 data⁵.

We adopted an absorbed optically-thin plasma with a minimum number of thermal components as best-fit model suitable to describe the observed spectrum reasonably well. The fit procedure was performed by linking the abundances of elements heavier than He together and leaving as free parameters the temperatures, the emission measures, the hydrogen column density, and the metallicity. After this initial step, we also left the abundances of individual elements as free parameters, which significantly improved the fit. The errors were estimated by checking $\Delta\chi^2$ while simultaneously varying all the best-fit parameters. In Table 4 we list parameters and errors of the best-fit models, and in Fig. 6 we display observed and predicted X-ray spectra.

The hydrogen column densities derived from X-ray spectral analysis range from 0.32 to $2.4 \times 10^{21} \text{ cm}^{-2}$. The average value, $\sim 1.5 \times 10^{21} \text{ cm}^{-2}$, was assumed for the spectra with low S/N . This N_{H} range is compatible with the values derived by Sciortino et al. (1998) from the analysis of *ROSAT*/PSPC spectra and is compatible with the A_V value of 0.1 – 0.8 estimated by Walter et al. (1994). The derived N_{H} does not vary too much from star to star suggesting that only a small contribution to the hydrogen column density is due to local circumstellar material.

4.3. X-ray flux and luminosity

From the best-fit models of the X-ray-brightest USco members we evaluated their unabsorbed X-ray flux and luminosity. These flux values were used to derive a mean conversion factor from PN equivalent count rate to flux of $2.37 \times 10^{-12} \text{ erg cm}^{-2}$ in the 0.5 – 8.0 keV energy band. By this factor we also derived X-ray fluxes for the faintest X-ray USco sources. This procedure relies on the hypothesis that plasma characteristics do not vary substantially from source to source. Since source 100 displays much harder spectra than other USco sources (see Sect. 4.1), we did not consider it for the conversion factor evaluation. The X-ray fluxes and luminosities of the photometric USco members are listed in Table 3.

5. Variability analysis

In this section we report the analysis of the short-term X-ray variability of photometric USco members, together with the detailed study of strong and isolated flares. Also long-term X-ray variability is investigated by comparing the *ROSAT* and *XMM-Newton* results.

5.1. Kolmogorov-Smirnov test

We studied the X-ray variability of all the detected sources by applying the unbinned Kolmogorov-Smirnov (KS) test. We analyzed the photon arrival times adding the PN, MOS1, and MOS2 data, because we aimed at maximizing the S/N of each source

Table 4. Fit results of the EPIC spectra of the Upper Scorpius members.

Source	Instrument ^a	N_{H} (10^{21} cm^{-2})	$\log T_1$ (K)	$\log T_2$ (K)	$\log T_3$ (K)	$\log EM_1$ (cm^{-3})	$\log EM_2$ (cm^{-3})	$\log EM_3$ (cm^{-3})	Fe ^b	O ^b	Ne ^b	$\chi^2/\text{d.o.f.}$
7	PN+M1+M2	$0.32^{+0.27}_{-0.25}$	$6.64^{+0.05}_{-0.05}$	$7.39^{+0.07}_{-0.06}$...	$52.98^{+0.34}_{-0.31}$	$53.26^{+0.06}_{-0.09}$...	$0.20^{+0.21}_{-0.11}$	= Fe	$1.12^{+1.11}_{-0.57}$	438.2/391
32	PN	= 1.50	$7.06^{+0.10}_{-0.10}$	$51.93^{+0.06}_{-0.07}$	= 0.15	= Fe	= Fe	8.5/11
42	PN+M1+M2	$1.38^{+0.89}_{-0.72}$	$6.55^{+0.14}_{-0.17}$	$6.99^{+0.09}_{-0.07}$...	$52.65^{+0.40}_{-0.43}$	$52.51^{+0.20}_{-0.25}$...	$0.14^{+0.14}_{-0.05}$	= Fe	= Fe	116.2/120
43	PN+M1+M2	$0.55^{+0.66}_{-0.50}$	$6.60^{+0.16}_{-0.14}$	$7.05^{+0.05}_{-0.07}$...	$52.79^{+0.37}_{-0.37}$	$52.82^{+0.20}_{-0.18}$...	$0.16^{+0.12}_{-0.08}$	= Fe	= Fe	132.7/126
62	PN+M1+M2	$0.88^{+0.50}_{-0.47}$	$6.96^{+0.04}_{-0.05}$	$52.42^{+0.15}_{-0.15}$	$0.08^{+0.08}_{-0.03}$	= Fe	= Fe	87.0/70
95	PN+M1+M2	$1.39^{+1.25}_{-0.69}$	$6.48^{+0.11}_{-0.14}$	$6.98^{+0.07}_{-0.06}$...	$52.88^{+0.48}_{-0.49}$	$52.79^{+0.18}_{-0.22}$...	$0.14^{+0.10}_{-0.05}$	= Fe	= Fe	138.4/110
100	PN+M1+M2	$1.30^{+0.44}_{-0.25}$	$6.46^{+0.13}_{-0.07}$	$7.24^{+0.06}_{-0.07}$	$7.91^{+0.16}_{-0.09}$	$53.77^{+0.55}_{-0.51}$	$53.76^{+0.17}_{-0.19}$	$54.01^{+0.06}_{-0.07}$	$0.27^{+0.09}_{-0.10}$	$0.13^{+0.24}_{-0.08}$	$0.48^{+0.84}_{-0.31}$	1494.8/1218
114	M1+M2	$1.97^{+0.66}_{-1.33}$	$6.72^{+0.21}_{-0.07}$	$7.48^{+0.72}_{-0.47}$...	$53.78^{+0.28}_{-0.91}$	$52.62^{+0.67}_{-0.49}$...	$0.05^{+0.15}_{-0.02}$	= Fe	$0.34^{+0.52}_{-0.16}$	149.4/120
125	PN	$2.18^{+2.20}_{-1.32}$	$6.51^{+0.11}_{-0.11}$	$7.09^{+0.07}_{-0.11}$...	$53.02^{+0.76}_{-0.68}$	$52.60^{+0.28}_{-0.34}$...	$0.27^{+0.17}_{-0.16}$	= Fe	= Fe	45.5/50
132	PN+M2	$1.56^{+0.66}_{-0.31}$	$6.58^{+0.03}_{-0.03}$	$7.05^{+0.13}_{-0.16}$	$7.42^{+1.54}_{-0.41}$	$53.61^{+0.38}_{-0.42}$	$53.44^{+0.40}_{-0.36}$	$53.47^{+0.15}_{-0.61}$	$0.21^{+0.15}_{-0.13}$	= Fe	$0.46^{+0.50}_{-0.35}$	633.0/602
158	PN+M1+M2	$1.49^{+0.34}_{-0.34}$	$6.61^{+0.04}_{-0.04}$	$7.04^{+0.07}_{-0.07}$	$7.38^{+0.28}_{-0.28}$	$53.26^{+0.43}_{-0.43}$	$53.16^{+0.27}_{-0.28}$	$53.16^{+0.53}_{-0.53}$	$0.22^{+0.12}_{-0.12}$	= Fe	$0.50^{+0.24}_{-0.24}$	766.0/670
173	PN+M1+M2	$1.23^{+0.34}_{-0.34}$	$6.62^{+0.13}_{-0.08}$	$7.05^{+0.03}_{-0.04}$	$7.46^{+0.28}_{-0.10}$	$52.60^{+0.43}_{-0.33}$	$52.78^{+0.34}_{-0.27}$	$52.77^{+0.11}_{-0.30}$	$0.35^{+0.22}_{-0.17}$	= Fe	= Fe	512.3/482
180	M1+M2	$2.38^{+0.62}_{-0.87}$	$6.70^{+0.09}_{-0.06}$	$7.39^{+0.35}_{-0.23}$...	$54.09^{+0.26}_{-0.76}$	$53.23^{+0.31}_{-0.36}$...	$0.01^{+0.14}_{-0.01}$	$0.09^{+0.82}_{-0.06}$	$0.21^{+0.34}_{-0.10}$	213.4/180

All the errors are at 68% confidence level.

^a Instruments whose spectra were considered in the best-fit procedure.

^b Abundances are referred to solar photospheric values of Anders & Grevesse (1989).

⁵ A column of bad pixels of MOS1, located exactly on the source position, probably affects the effective area estimation.

Table 5. Number of variable sources derived from the Kolmogorov-Smirnov test.

Conf. Lev.	All sources		USco members	
	N_{var}	$N_{\text{var}}/N_{\text{tot}}$	N_{var}	$N_{\text{var}}/N_{\text{tot}}$
90%	42	18.8%	14	63.6%
99%	19	8.5%	13	59.1%

and therefore at increasing the diagnostic power for the weakest sources. The joint use of different instruments, reasonable because they share the same energy band, was performed by intersecting the good time intervals of the three instruments. This procedure has the advantage of increasing the total counts of each source by a factor ~ 2 , losing only 10% of the time coverage, mainly due to the lower PN exposure⁶.

Since the KS test probes unbinned arrival times, it does not distinguish between source and background photons. Thus to check background variability we also applied the KS test to the background events of each source.

We adopted the confidence levels of 90% and 99% for testing the hypothesis of constant emission. Table 5 reports the results for the sample of all detected X-ray sources and for the selected subset of photometric USco members. Among the sources that turned out to be variable at 99%, we discarded source 97 (not an USco member) because its variability is due to contamination: source 97 is located near the strong source 100, characterized by an intense flare (see Sect. 5.2), whose large point-spread function affects the photons extracted in the source 97 region. Some of the sources that are variable at 90% confidence level have a local background variable at the same confidence level; however, we did not discard them because the cumulative functions of source and background photon arrival times do not appear to be similar.

As indicated in Table 5 we found 13 USco stars variable at 99% (i.e. 59.1% of the detected USco members). In Fig. 7 we present the light curves of these 13 USco members. We plotted light curves without background subtraction. These 13 X-ray variable USco sources are also the 13 X-ray brightest ones among the 22 USco members. The weakest of this subsample is source 32, which has 290 EPIC net counts. Therefore our results are very likely influenced by statistics, and the estimated fraction of USco variable sources represents a lower limit.

The X-ray emission of the USco brown dwarf (source 45, 247 total EPIC counts, ~ 140 of which are background) does not display significant variability, suggesting that the observed X-rays are probably not due to isolated and bright flaring events.

5.2. Flare analysis

Figure 7 shows that the four sources 7, 32, 100, and 173 display intense and isolated flare events. The most intense flare was detected from source 100, whose count rate increased by a factor 100 during the flare. Source 7 shows a peculiar behavior: after the flare maximum the source reaches a quiescent emission higher by a factor ~ 2 than before the flare. A similar light curve was reported by Tsuboi et al. (1998) who observed the X-ray emission from the WTTS V773, indicating hence that this kind of flare may be common on non-accreting PMS stars.

The analysis of flares allows one to infer the length of the flaring structure. We adopted the method proposed by Reale et al. (1997) and recently used by Favata et al. (2005). In this section we apply this method to the flares of sources 7, 100, and 173,

⁶ The start of the PN detector is usually delayed a few ks (~ 2.5 in our cases) with respect to the two MOS detectors.

in order to infer characteristic lengths and heating properties of these flaring coronal structures.

Source 132 shows a slow decline during the entire observation (see Fig. 7). Different phenomena may produce this light curve: the superposition of small-amplitude variability, rotational modulation, or the decay of a flare. We made this last hypothesis, assuming therefore that the observation start coincided with the flare maximum and that the subsequent decline was the flare decay. Hence we performed, also for this source, time-resolved spectral analysis to derive the length of the flaring loop. We have no means of proving the correctness of this assumption, so that all the derived results depend on the validity of this hypothesis.

The Reale et al. method relies on the dependence of flaring-loop cooling on its length: the longer the decay, the longer the loop. The flare decay is also regulated by the amount of energy released into the loop itself after the flare maximum. This amount can be probed by studying the evolution of the plasma temperature and density during the flare decay.

There are three assumptions in the Reale et al. method: the flaring structure is a semicircular and symmetric coronal loop with uniform cross section, and its geometry does not change significantly during the flare; the plasma is confined inside the flaring loop; the plasma motion and the energy transport can occur only along the magnetic field. Under these assumptions it is possible to derive the loop length from the relation

$$L_9 = \frac{\tau_{\text{LC}} \sqrt{T_7}}{120f(\zeta)} \quad (1)$$

where L_9 is the loop semi-length in 10^9 cm, τ_{LC} the decay time in seconds of the light curve; T_7 is the peak temperature reached during the flare, in units of 10^7 K, and ζ is the slope of the trajectory followed by the flaring plasma in the $\log T$ vs. $\log N_e$ space during the decay. Under the hypothesis of constant volume of the flaring structure, the electron density N_e is proportional to the square root of the emission measure EM . The function $f(\zeta)$ takes the amount of heating released into the loop during the decaying phases into account, and it is defined as the ratio between the spontaneous thermodynamic loop decay τ_{th} and that measured from the light curve τ_{LC} . Note that $f(\zeta)$ depends on the instrument used to observe the flare X-ray emission. The calibrated $f(\zeta)$ function for the EPIC/PN detector, provided by Reale et al. (2004), is:

$$f(\zeta) = \frac{\tau_{\text{LC}}}{\tau_{\text{th}}} = a_1 \exp(-\zeta/a_2) + a_3 \quad (2)$$

with $a_1 = 11.6$, $a_2 = 0.56$, and $a_3 = 1.2$.

5.2.1. Fitting procedure

All the physical quantities contained in Eq. (1) refer to the loop where the flare occurred. To separate the X-ray emission of the quiescent corona from that of the flaring structure, we estimated a model that describes the quiescent phase preceding, or succeeding, the flare, assuming that this quiescent component did not change during the flare (for the selection of the source 132 quiescent phase see Sect. 5.2.4). Thus we fitted the EPIC spectra of the flaring phases adding to the model of the quiescent corona another thermal component, which takes only the flaring loop into account. We fitted the quiescent phase with an absorbed, optically-thin plasma with 1 or 2 thermal components, with all the abundances of elements heavier than He tied together. For

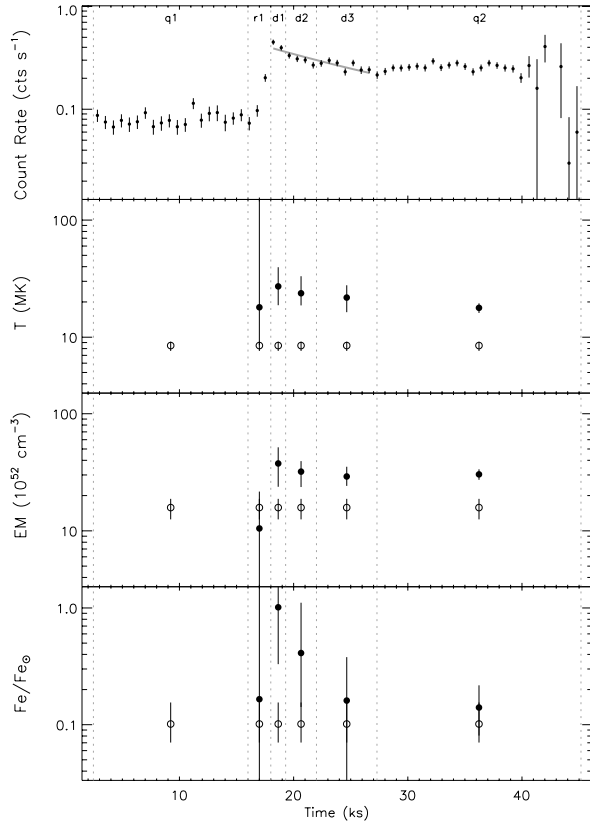


Fig. 8. Flare analysis of source 7. *Upper panel:* background-subtracted light curve obtained by binning PN arrival times with a bin of 700 s; the solid gray line represents the best-fit exponential decay. *Lower panels:* plasma temperature, emission measure, and metallicity (referred to Anders & Grevesse 1989) derived from spectral fitting of each time interval; open symbols mark the quiescent component, filled symbols the flaring component.

all the flaring phases, we added a further absorbed optically-thin isothermal plasma to the above quiescent model with all the abundances of elements heavier than He tied to Fe. In the best-fit procedure all the parameters of the quiescent model were kept frozen. We instead left as free parameters the temperature, emission measure, and metallicity of the added flaring model. In all cases, we found that the hydrogen column density N_{H} remains constant and compatible with the value estimated from the analysis of the whole spectrum (see Table 4), hence it was kept frozen. The error estimation was performed by studying the $\Delta\chi^2$ while changing all the best-fit parameters simultaneously.

5.2.2. Source 7

Source 7 is an M1.5 WTTS with $M_{\star} \approx 0.3 M_{\odot}$ and $R_{\star} \approx 2.3 R_{\odot}$ (Adams et al. 1998). Its X-ray light curve is plotted in the upper panel of Fig. 8. We divided the whole observation into six intervals. The quiescent spectrum is collected during the “q1” interval. The results of the best-fit are displayed in the lower panels of Fig. 8 and listed in Table A.1. Significant abundance variations were registered: the flaring plasma reaches an abundance similar to the solar photospheric value, while the quiescent coronal plasma is heavily metal-depleted.

The decay time of the flare was derived by fitting the count rates in the d1, d2, and d3 intervals, assuming an exponential function plus a constant as best-fit model. The constant (0.08 cts s^{-1}), representing the quiescent X-ray emission,

was obtained as the average count rate value of the quiescent phase q1. The derived exponential decay of the best-fit function (shown in the upper panel of Fig. 8) is $\tau_{\text{LC}} = 11.1 \pm 1.3 \text{ ks}$.

5.2.3. Source 100

Counterpart of source 100 is HD 142578, whose optical photometry (Slawson et al. 1992) suggests $M_{\star} \sim 2 M_{\odot}$ and $R_{\star} \sim 3 R_{\odot}$. The XMM-Newton observation of field 2, which contains source 100, is affected by high background levels especially in the last $\sim 5 \text{ ks}$ of the exposure. Hence the time screening procedure made us discard mainly the last section of the observation, as can be seen from the light curves contained in the left column of Fig. 7. The flare of source 100 occurred $\sim 30 \text{ ks}$ after the observation start, and only the first decay phases were recorded. To optimize the analysis of the flare decay, we considered the whole observation exposure without applying any time screening. The high background level registered in the last part of the field 2 observation does not heavily affect the analysis of source 100 because the source count rate is much higher than the background count rate.

In the upper panel of Fig. 9 we display the background-subtracted PN light curve of source 100 extracted from the un-screened field 2 observation. We divided the observation into 10 intervals. Both the quiet and flaring emission are described well by an absorbed 1- T thermal component. The results for the evolution of temperature, emission measure, and global abundance are reported in the lower panels of Fig. 9 and in Table A.2. Also in this case we registered a significant abundance increase: the flaring plasma shows a higher metallicity than the quiescent one by a factor ~ 20 . A flare decay time of $15.4 \pm 0.4 \text{ ks}$ was obtained by fitting the d1–d4 intervals (see Fig. 9).

5.2.4. Source 132

Source 132 is a K0 young star, whose N -band excess and asymmetric $H\alpha$ features suggest it is actively accreting material from its circumstellar disk (Mamajek et al. 2004). From the L_{bol} and T_{eff} values derived by Preibisch & Zinnecker (1999), we deduce $R_{\star} \sim 3.5 R_{\odot}$. The upper panel of Fig. 10 shows the background-subtracted PN light curve of source 132. The decay phase lasts for the first $\sim 30 \text{ ks}$, after which variability with smaller amplitude affects the emission.

After inspection of the light curve, we divided the whole observation into 9 segments, as indicated in Fig. 10. To determine the interval to adopt for the quiescent emission we evaluated the hardness ratio $HR = (H-S)/(H+S)$ of each interval, where S indicates the number of photons detected in the 0.3–1.5 keV band, and H those in the 1.5–7.9 keV band. The results are displayed in the second panel of Fig. 10. We chose the interval with the softest spectrum for estimating the quiescent model, noting that this interval, named q1, also shows the minimum count rate.

We checked that the abundance of the flaring plasma did not vary and was compatible with that of the quiescent model. We therefore kept it fixed to the value derived from the analysis of the whole spectrum: $\text{Fe} = 0.21 \text{ Fe}_{\odot}$. In the lower panels of Fig. 10 we report the best-fit values of temperature and emission measure for each explored time interval. All the best-fit parameters are also listed in Table A.3. The hypothesis of a flare decay to describe the observed light curve is supported by the decrease in the observed temperature. The decay time ($11.4 \pm 1.3 \text{ ks}$) of the light curve was estimated by fitting the observed count rates of the d1–d4 intervals.

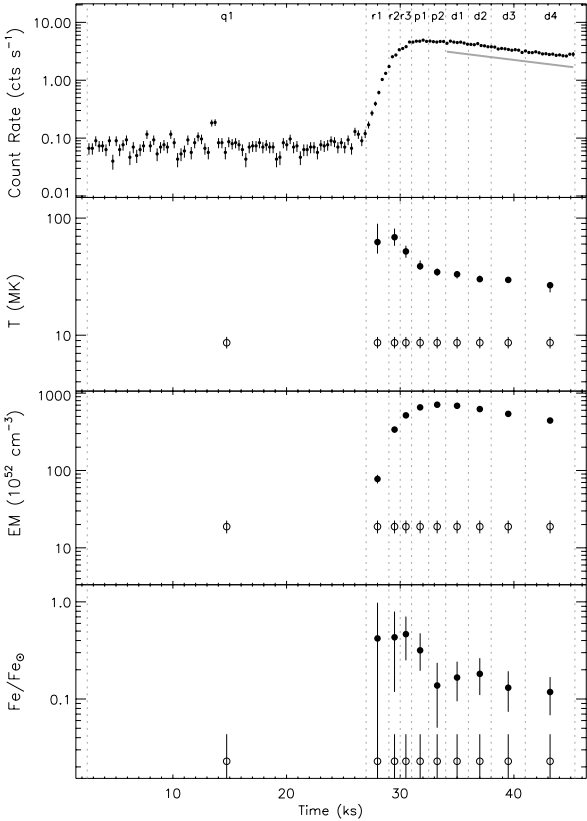


Fig. 9. Flare analysis of source 100. *Upper panel:* background-subtracted light curve obtained by binning PN arrival times with a bin of 300 s; the solid gray line represents the exponential decay (reduced by a factor 1.5 to make it visible) obtained from best-fit of count rates in the d1, d2, d3, and d4 intervals. *Lower panels:* plasma temperature, emission measure, and metallicity derived from spectral fitting of each time interval; open symbols mark the quiescent component, filled symbols the flaring component.

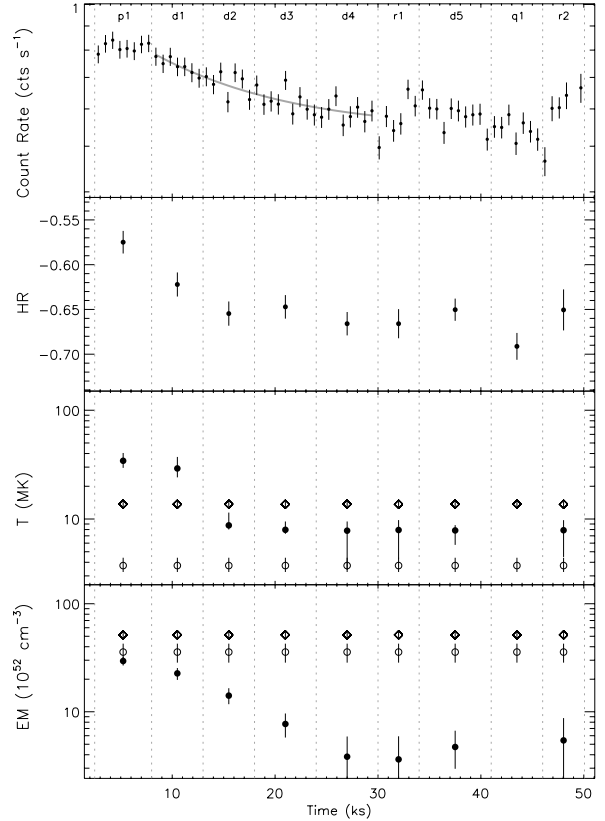


Fig. 10. Flare analysis of source 132. *From upper to lower panel:* background-subtracted PN light curve with a bin of 700 s, the solid gray line represents the exponential decay obtained from best-fit of count rates in the d1, d2, d3, and d4 intervals; hardness ratio $HR = (H-S)/(H+S)$, with S and H indicating the number of photons detected in the 0.3–1.5 and 1.5–7.9 keV bands, respectively; plasma temperature, emission measure, and metallicity derived from spectral fitting of each time interval; open symbols mark the quiescent component, filled symbols the flaring component.

5.2.5. Source 173

No bibliographic information is available for the 2MASS and DENIS counterparts of source 173, which we selected as a photometric USco member for the first time. The 2MASS $H - K$ color and the Siess et al. (2000) models indicate $R_{\star} \sim 1 R_{\odot}$. The background-subtracted PN light curve of source 173 is shown in the upper panel of Fig. 11. However the PN observation started when the flare was already in the decay phase. To determine the length of the flaring structure, we need to measure the maximum temperature of the plasma during the flare (see Eq. (1)). With this aim we inspected the MOS1 and MOS2 data because their observation started ~ 2.5 ks before that of the PN detector. In the upper panel of Fig. 11 we also report the background-subtracted light curve obtained by adding MOS1 and MOS2 photon arrival times. From the comparison of PN and MOS light curves, it emerges that the PN detector missed a significant fraction of the flare evolution. We assume that the MOS data started just after the flare maximum. However, since the maximum temperature is usually reached during the rising phases (see the temperature evolution of source 100 shown in Fig. 9) we are most likely determining a lower limit.

We divided the PN observation into 6 intervals, as reported in Fig. 11, with another interval that probes the flare peak from the MOS data with a duration of 1 ks. The quiescent emission

was estimated from the constant level reached after the flare end (q1 interval).

Global metal abundance remains constant during the whole observation, so that we performed the spectral fitting leaving it fixed to the values of $Fe/Fe_{\odot} = 0.35$ (see Table 4). The best-fit results are shown in the lower panels of Fig. 11 and listed in Table A.4. The best-fit function of the flare decay (d1, d2, and d3 intervals) has a decay time τ_{LC} of 3.96 ± 0.15 ks (upper panel of Fig. 11).

5.2.6. Loop length estimation

To estimate the size of the flaring loops we need to determine the slope of the path described in the density vs. temperature plane by the plasma during the cooling phases. With the hypothesis of a constant volume of the loop, the emission measure is proportional to the square of the electron density.

In Fig. 12 we show the evolution of $\log T$ and $0.5 \log EM$ for the flares analyzed. For each flare we only report the points regarding the decay phases. In all the cases, the hypothesis of a linear trajectory is verified. We performed linear regression of the plotted points. The estimated slopes ζ are 1.7 ± 4.6 , 1.0 ± 0.4 , 3.6 ± 1.2 , and 0.43 ± 0.12 for the source 7, 100, 132, and 173, respectively. Then we evaluated $f(\zeta)$ by applying Eq. (2). In Table 6 we report the measured ζ and the corresponding $f(\zeta)$.

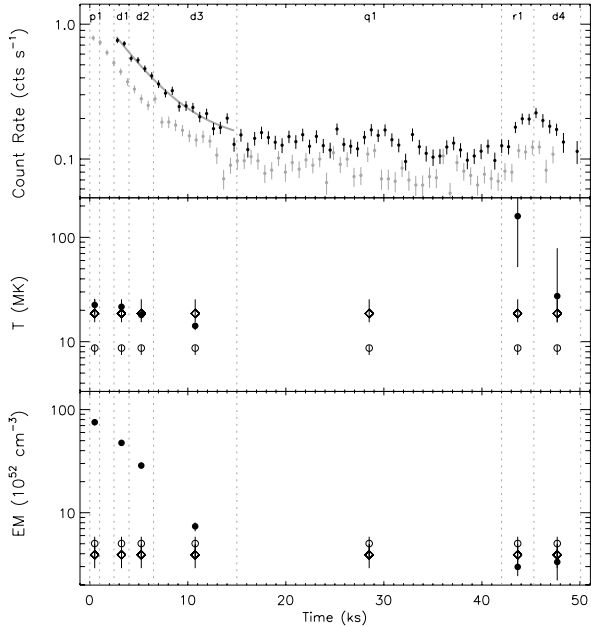


Fig. 11. Flare analysis of source 173. *Upper panel:* background-subtracted PN light curve (black) and MOS light curve (gray) obtained with a bin of 700 s; the solid gray line represents the best-fit exponential decay. *Lower panels:* plasma temperature and emission measure derived from spectral fitting of each time interval; open symbols mark the quiescent component, filled symbols the flaring component. All the best-fit results refer only to PN data analysis, except for fit results of the p1 interval that were obtained from MOS data (more details can be found in Sect. 5.2).

The large $f(\zeta)$ values obtained for sources 100 and 173 suggest the presence of sustained heating.

To evaluate the loop maximum temperature experienced during the flare we converted the measured maximum temperature adopting the relation

$$T_{\text{peak}} = 0.184 T_{\text{obs}}^{1.130}$$

where T_{peak} and T_{obs} are expressed in K (Reale et al. 2004). Both T_{obs} and T_{peak} are listed in Table 6.

The estimated loop semi-lengths for sources 7, 100, 132, and 173 are ~ 0.7 , ~ 0.7 , ~ 0.8 , and ~ 0.14 of stellar radii (see Table 6). Starting from the loop size we derive indications of the plasma density and magnetic field. We define β as the ratio between the section radius r and the loop semi-length L . The loop volume is therefore:

$$V_{\text{loop}} = 2\pi\beta^2 L^3 \quad (3)$$

Considering the highest value of EM and the loop volume given by (3), we can evaluate the peak density reached by the plasma:

$$N_e = \sqrt{\frac{EM_{\text{max}}}{0.8 \cdot 2\pi\beta^2 L^3}} \quad (4)$$

where N_e is the electron density, and the factor 0.8 is assumed as the ratio between N_H and N_e . From density and temperature we can estimate the pressure. Since the confinement of the plasma into the loop is due to the magnetic field, we can infer the minimum magnetic field needed to constrain the plasma, when it reaches the maximum pressure during the flare. The magnetic field B in Gauss is given by:

$$B = \sqrt{8\pi k_2 (N_e T)_{\text{max}}} \quad (5)$$

Table 6. Results of loop length analysis.

USco star	7	100	132	173
Stellar properties				
V	13.01 ^a	8.63 ^b
$B - V$	1.47 ^a	0.23 ^b
$R_{\star} (R_{\odot})$	2.3 ^c	~ 3 ^d	~ 3.5 ^e	~ 1 ^f
Flaring loop properties				
$T_{\text{obs}} \text{ (MK)}$	27 ± 10	69 ± 12	34 ± 5	23 ± 3
$T_{\text{peak}} \text{ (MK)}$	46 ± 20	132 ± 25	60 ± 11	38 ± 6
ζ	1.7 ± 4.6	1.0 ± 0.4	3.6 ± 1.2	0.43 ± 0.12
$f(\zeta)$	1.7 ± 4.3	3.2 ± 1.5	1.22 ± 0.04	6.5 ± 1.2
$\tau_{\text{LC}} \text{ (ks)}$	11.1 ± 1.3	15.4 ± 0.4	11.4 ± 1.3	3.96 ± 0.15
$L (10^{10} \text{ cm})$	~ 11	15 ± 7	19 ± 3	0.98 ± 0.19
$L (R_{\star})$	~ 0.7	~ 0.7	~ 0.8	~ 0.14
$N_e (10^{10} \text{ cm}^{-3})$	~ 7.0	~ 21	~ 3.8	~ 400
$B \text{ (G)}$	~ 150	~ 370	~ 110	~ 1000

The electron density N_e of the flaring loop is evaluated as $\sqrt{EM_{\text{max}}/(0.8 \cdot 2\pi\beta^2 L^3)}$, assuming $\beta = 0.1$. The magnetic field values B represent the minimum values needed to confine the flaring plasma at the maximum pressure and are evaluated as $\sqrt{8\pi P_{\text{max}}}$, with $P_{\text{max}} = k_2(N_e T)_{\text{max}}$. ^a From Walter et al. (1994). ^b From Slawson et al. (1992). ^c From Adams et al. (1998). ^d Estimated from the $B - V$ color and the Siess et al. (2000) models. ^e Estimated from the L_{bol} and T_{eff} values derived by Preibisch & Zinnecker (1999). ^f Estimated from the $H - K$ 2MASS color and the Siess et al. (2000) models.

Solar coronal loops usually display $\beta \approx 0.1$, while in some active stars higher values ($\beta \approx 0.3$) were inferred (Favata et al. 2000a). Assuming $\beta = 0.1$ we derived the values listed in Table 6. The density N_e and the magnetic field B are evaluated considering the highest values of EM and P , respectively, which usually did not occur in the same time interval. Magnetic field values higher than a few 10^2 G are compatible with the photospheric values typical of young late type stars (Guenther et al. 1999; Symington et al. 2005).

5.3. Long-term variability: comparison with ROSAT results

The field 2 was previously observed with a pointed ROSAT/PSPC observation in 1993 (Sciortino et al. 1998), so the comparison between XMM-Newton and ROSAT data allows us to search long-term X-ray variability of USco members.

Sciortino et al. (1998) evaluated X-ray luminosity in the 0.2–2.0 keV energy band assuming a distance of 160 pc, leading us to scale the ROSAT/PSPC luminosity to a distance of 145 pc. We evaluated L_X from XMM-Newton data in the 0.2–2.0 keV energy band by converting the measured X-ray count rate to an unabsorbed energy flux by the conversion factor $2.71 \times 10^{-12} \text{ erg cm}^{-2} \text{ cts}^{-1}$ (the procedure adopted to estimate this conversion factor is explained in Sect. 4.3).

To also check for long-term variability for USco members of field 1, we searched those included in the ROSAT All Sky Survey Bright Source Catalog (RASS-BSC, Voges et al. 1999), performed in 1990–1991. We found RASS-BSC counterparts for sources 114 and 132. Starting from the RASS-BSC count rate and HRI , we evaluated their X-ray fluxes in the 0.1–2.4 keV band by adopting the method of Fleming et al. (1995). Then we applied a conversion factor of 0.80, evaluated with PIMMS V3.6c⁷, to convert this flux from the 0.1–2.4 keV into the

⁷ The PIMMS count rate simulator is accessible via URL at <http://heasarc.gsfc.nasa.gov/Tools/w3pimms.html>

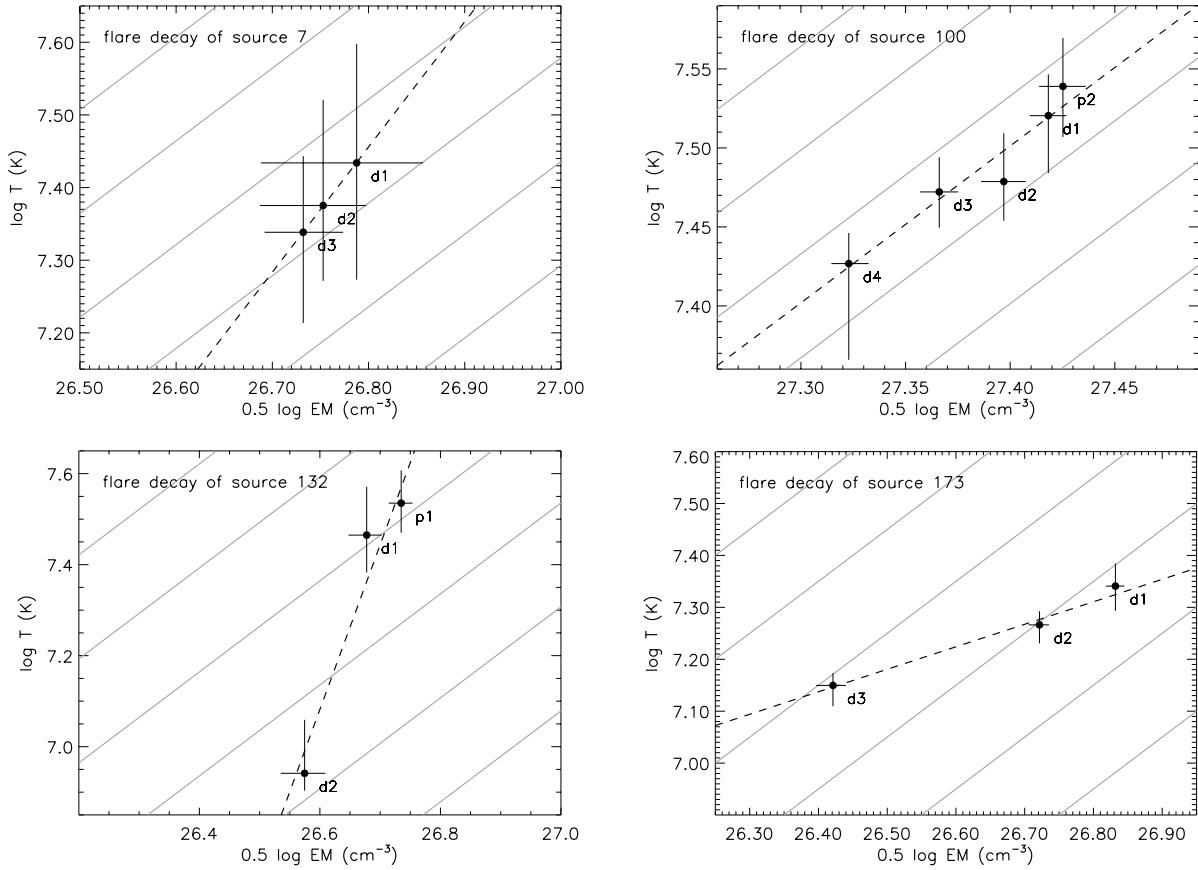


Fig. 12. Evolution of the flare decaying phases in the temperature vs. density diagram ($0.5 \log EM \propto \log N_e$, where N_e is the electron density). Dashed black lines mark the linear best-fit model, solid gray lines indicate lines with slope 1.

0.2–2.0 keV band. The comparison between the *ROSAT* and *XMM-Newton* X-ray luminosities is shown in Fig. 13.

All the sources, except for source 100, present X-ray luminosity variations smaller than a factor 3; the X-ray luminosity of source 100 measured by *ROSAT* is much lower than what we measured in the *XMM-Newton* observation, but this difference is entirely due to the flare, in fact the *ROSAT* X-ray luminosity is compatible with the quiescent X-ray luminosity of source 100 ($\log L_X = 30.0$ in the 0.2–2.0 keV band).

6. Discussion and conclusions

In the analyzed *XMM-Newton* observations, we detected and identified 22 photometric USco members with masses ranging from ~ 0.05 to $\sim 2 M_\odot$. This stellar sample includes 1 CTTS and 7 WTTSs, while no indication is available for the remaining 14 members. Since the CTTSs frequency in the USco association is very low (~ 2 –5%) (Walter et al. 1994; Martin 1998), it is conceivable that source 132 is the only CTTS in our sample. In the following discussion, the sample of 22 USco members detected in this X-ray survey is considered as a whole, since no significant differences between the X-ray properties of the CTTS source 132 and the other members were found.

6.1. X-ray luminosity

We explored how the X-ray luminosity of the USco members changes with NIR colors. We plot in Fig. 14 L_X vs. NIR colors obtained from the 2MASS and DENIS counterparts and also show in the two plots the locus of X-ray emission at the saturated

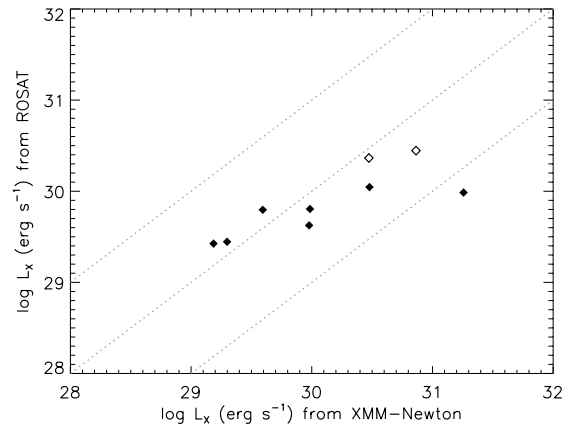


Fig. 13. Comparison between the X-ray luminosity of USco members, measured in the 0.2–2.0 keV band, by *ROSAT/PSPC* and *XMM-Newton*. Filled diamonds mark USco stars whose *ROSAT* X-ray luminosity was estimated by Sciortino et al. (1998) from a pointed observation. Open diamonds indicate USco members whose *ROSAT* X-ray luminosity was estimated from the RASS data.

level, $\log L_X/L_{\text{bol}} = -3$, predicted using the evolutionary models of Siess et al. (2000) and Baraffe et al. (1998).

For some of the X-ray-detected USco members, stellar parameters are available from literature: we list them in Table 7. For this subset of USco members we plot the X-ray luminosity vs. bolometric luminosity (Fig. 15), confirming the saturated X-ray emission of USco stars.

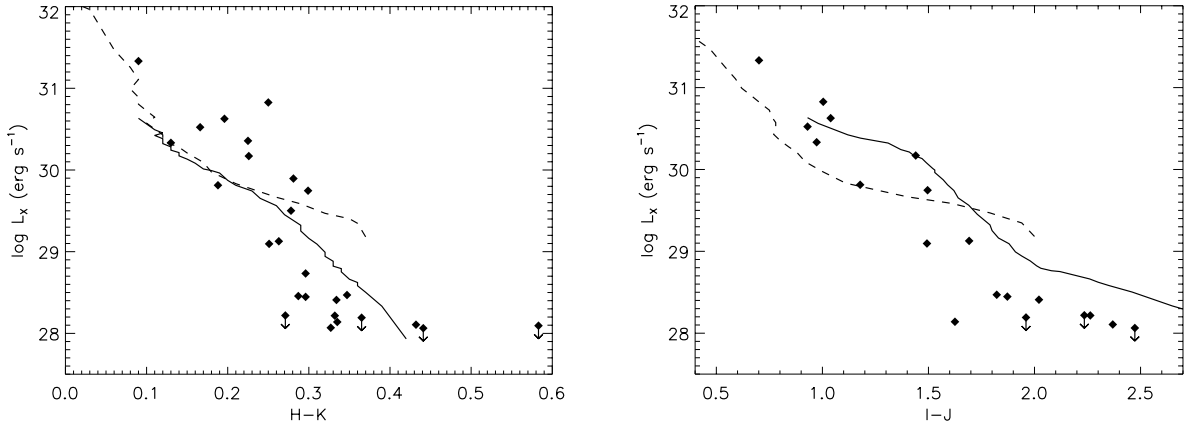


Fig. 14. X-ray luminosity of USco members vs. $H - K$ (left panel) and $I - J$ (right panel) colors obtained from the 2MASS and DENIS catalogs. Dashed and solid lines represent the saturated level ($\log L_X/L_{\text{bol}} = -3$) predicted by the Siess et al. (2000) and Baraffe et al. (1998) models, respectively.

Table 7. Stellar parameters.

Source	Simbad	$\log L_{\text{bol}}/L_{\odot}$	Ref
7	V* V1144 Sco	-0.25	W94
43	V* V1146 Sco	-0.397	P99
45	DENIS-P J155601.0-233808	-2.08	B04
95	V* V1145 Sco	-0.89	W94
114	GSC 06793-00569	0.215	P99
132	GSC 06793-00819	0.736	P99
158	GSC 06793-00994	0.297	P99
180	GSC 06793-00797	0.257	P99
	UScoCTIO 104	-1.959	M04

In the reference column W94, P99, B04 and M04 designate Walter et al. (1994), Preibisch & Zinnecker (1999), Bouy (2004) and Mohanty et al. (2004), respectively.

6.2. Coronal plasma properties

We evaluated the effective coronal temperature⁸ of those stars whose spectra were analyzed, which ranges from 6 to 40 MK ($\log T(\text{K}) = 6.8-7.6$). These values are compatible with those of the WTTSs of the younger ρ Oph cloud (Ozawa et al. 2005), of the L1551 region (Favata et al. 2003), and of the Orion Molecular Cloud 2 and 3 (Tsujiimoto et al. 2002). It suggests that the characteristic temperature of the plasma responsible for the X-ray emission in WTTS does not evolve significantly during the PMS stages. The PMS stars in the Orion nebula cluster show increasing coronal temperature for increasing photospheric temperature (Preibisch et al. 2005). Instead, our results do not suggest any correlation of coronal temperatures with NIR colors, possibly because of the smaller stellar sample.

All the USco stars whose X-ray spectra were analyzed showed elemental abundances reduced with respect to the solar photospheric values. The global metallicity is in all cases ≤ 0.35 in solar units. Moreover Ne, when estimated independently from Fe, turned out to be less depleted than Fe. The Ne/Fe ratio ranges from 2 to 17 times the solar photospheric ratio. As in the case of coronal temperatures, coronal metallicity also does not show any significant trend with respect to NIR colors, meaning that the photospheric temperature does not seem to affect the metal depletion of coronal plasma.

⁸ Defined as the weighted average of the best-fit temperatures, adopting the relevant emission measures as weight.

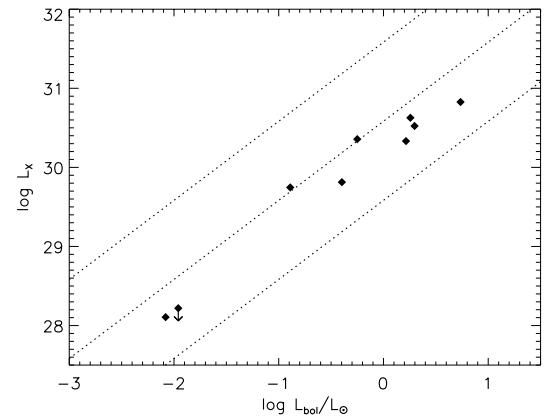


Fig. 15. Fractional X-ray luminosity vs. bolometric luminosity. Dotted lines represent X-ray to bolometric luminosity ratios of 10^{-2} , 10^{-3} , and 10^{-4} .

6.3. Short term X-ray variability

We find that 13 of the 22 photometric USco members were variable during the observations. Since the 13 variable sources are also the X-ray brightest, our result is very likely biased by the quality of the X-ray data collected.

Analysis of the four strongest and isolated flares produced by USco members displayed very hot plasmas with temperatures as high as 70 MK and peak luminosity up to 8×10^{31} erg s⁻¹. We derived the flaring loops semi-length finding that these sizes were slightly smaller than the stellar radius ($L \sim 0.7-0.8 R_{\star}$) in three cases, while in the last case the flare originated in a compact loop with semi-length of $L \sim 0.1 R_{\star}$. These results are supported by studies of X-ray flares performed adopting different methods (Favata et al. 2001; Imanishi et al. 2003; Grosso et al. 2004). As a result, coronal loops longer than the stellar radius, such as those found in the Orion nebula cluster by Favata et al. (2005), are rare and/or present only in the very early stages of stellar evolution. However, the flares studied by Favata et al. (2005) have very long duration (with a time decay of $\sim 10-10^2$ ks), and they may escape detection in observations with short exposure times.

The intermediate-mass star HD 142578 (source 100, the most X-ray luminous in Fig. 14) displays an X-ray luminosity, evaluated over the entire observation, near the saturated level, which is not expected for an A2 young star. During the

observation a large flare occurred, with the count rate rising up to a factor 100 in a few ks. The X-ray luminosity evaluated in the quiescent phase is $\log L_X = 29.8$. Assuming that the X-ray emitter is an unresolved low-mass companion characterized by a saturated X-ray emission (hence $L_{\text{bol}} = 0.16 L_{\odot}$), the Siess et al. (2000) model predicts $M_{\star} \sim 0.4 M_{\odot}$ and $R_{\star} \sim 1 R_{\odot}$ for it. Under this hypothesis the length of the flaring loop should have been $2 R_{\star}$, and the X-ray luminosity during the flare should have reached $\sim 10\%$ of the bolometric luminosity. Such high X-ray to bolometric ratios during flares were already observed (e.g. Favata et al. 2000b).

The flare analysis of source 7 and 100 has shown that the plasma metallicity is higher in the flaring structures than in the quiet coronal plasma. Abundance variations during flares were observed in some cases (Tsuboi et al. 1998; Güdel et al. 1999; Favata & Schmitt 1999; Güdel et al. 2001; Imanishi et al. 2002), where metal enrichment up to a factor ~ 5 was registered. The metallicity of the flaring plasma of source 100 was enhanced by a factor ~ 20 compared to the quiescent plasma.

The general view suggested for the abundance variation during flares invokes evaporation of photospheric material that then fills the flaring structures. If the mechanism responsible for the FIP or inverse FIP effect in quiescent coronal structures acts on longer time scales than the characteristic rise times of coronal flares (few ks), it is conceivable that the evaporated photospheric material radiates X-ray emission before being affected by any FIP-related effect. Therefore the abundances of the flaring structures may reflect the chemical composition of the underlying stellar photosphere.

In this scenario we infer that the quiescent corona is actually metal-depleted compared to the underlying photosphere; on the other hand, since the flaring composition reaches the highest value of $\text{Fe}/\text{Fe}_{\odot} \sim 0.5\text{--}1$, we conclude that PMS stars of the USco association do have solar-like composition.

Note that the abundance increase during strong flares is followed by an abundance decrease just after the flare maximum. This effect is visible in the flare analysis of sources 7 and 100 reported in Figs. 8 and 9. In both cases the abundance decays on time scales of $\sim 1\text{--}2$ ks, much faster than the characteristic time (36 ks) of the abundance decay observed in a flare of Algol (Favata & Schmitt 1999), which did show much longer decay time (50 ks). While it is conceivable that the rapid evaporation of photospheric material may produce the observed rise of metallicity on very short time scales, it is difficult to explain how the newly evaporated plasma is so efficiently depleted of heavy elements on such short time scales.

Acknowledgements. We would like to thank F. Reale for the useful discussion of flare analysis and I. Pillitteri for helpful suggestions on the procedure of X-ray source detection. C.A., E.F., A.M., G.M., G.P., and S.S. acknowledge partial support for this work from contract ASI-INAF I/023/05/0 and from the Ministero dell'Istruzione, Università e Ricerca. Based on observations obtained with XMM-Newton, an ESA science mission with instruments and contributions directly funded by ESA Member States and NASA.

References

- Adams, N. R., Walter, F. M., & Wolk, S. J. 1998, *AJ*, 116, 237
 Alexander, D. M., Bauer, F. E., Brandt, W. N., et al. 2003, *AJ*, 126, 539
 Anders, E., & Grevesse, N. 1989, *Geochim. Cosmochim. Acta*, 53, 197
 Ardila, D., Martín, E., & Basri, G. 2000, *AJ*, 120, 479
 Baraffe, I., Chabrier, G., Allard, F., & Hauschildt, P. H. 1998, *A&A*, 337, 403
 Bouvier, J., Cabrit, S., Fernandez, M., Martin, E. L., & Matthews, J. M. 1993, *A&A*, 272, 176
 Bouy, H. 2004, *A&A*, 424, 619
 Damiani, F., Maggio, A., Micela, G., & Sciortino, S. 1997a, *ApJ*, 483, 350
 Damiani, F., Maggio, A., Micela, G., & Sciortino, S. 1997b, *ApJ*, 483, 370
 de Bruijne, J. H. J., Hoogerwerf, R., Brown, A. G. A., Aguilar, L. A., & de Zeeuw, P. T. 1997, in *ESA SP-402: Hipparcos – Venice '97*, 575
 de Geus, E. J. 1992, *A&A*, 262, 258
 de Geus, E. J., de Zeeuw, P. T., & Lub, J. 1989, *A&A*, 216, 44
 Favata, F., & Schmitt, J. H. M. M. 1999, *A&A*, 350, 900
 Favata, F., Micela, G., & Reale, F. 2000a, *A&A*, 354, 1021
 Favata, F., Reale, F., Micela, G., et al. 2000b, *A&A*, 353, 987
 Favata, F., Micela, G., & Reale, F. 2001, *A&A*, 375, 485
 Favata, F., Fridlund, C. V. M., Micela, G., Sciortino, S., & Kaas, A. A. 2002, *A&A*, 386, 204
 Favata, F., Giardino, G., Micela, G., Sciortino, S., & Damiani, F. 2003, *A&A*, 403, 187
 Favata, F., Flaccomio, E., Reale, F., et al. 2005, *ApJS*, 160, 469
 Feigelson, E. D., & Montmerle, T. 1999, *ARA&A*, 37, 363
 Flaccomio, E., Favata, F., Micela, G., & Sciortino, S. 2000, in *ESA SP-445*
 Flaccomio, E., Micela, G., & Sciortino, S. 2003a, *A&A*, 397, 611
 Flaccomio, E., Micela, G., & Sciortino, S. 2003b, *A&A*, 402, 277
 Flaccomio, E., Micela, G., & Sciortino, S. 2006, *A&A*, in press
 [arXiv:astro-ph/0604243]
 Fleming, T. A., Molendi, S., Maccacaro, T., & Wolter, A. 1995, *ApJS*, 99, 701
 Grosso, N., Montmerle, T., Feigelson, E. D., & Forbes, T. G. 2004, *A&A*, 419, 653
 Güdel, M., Linsky, J. L., Brown, A., & Nagase, F. 1999, *ApJ*, 511, 405
 Güdel, M., Audard, M., Briggs, K., et al. 2001, *A&A*, 365, L336
 Guenther, E. W., Lehmann, H., Emerson, J. P., & Staude, J. 1999, *A&A*, 341, 768
 Hartmann, L., Hewett, R., & Calvet, N. 1994, *ApJ*, 426, 669
 Imanishi, K., Tsujimoto, M., & Koyama, K. 2002, *ApJ*, 572, 300
 Imanishi, K., Nakajima, H., Tsujimoto, M., Koyama, K., & Tsuboi, Y. 2003, *PASJ*, 55, 653
 Jayawardhana, R., Ardila, D. R., Stelzer, B., & Haisch, K. E. 2003, *AJ*, 126, 1515
 Köhler, R., Kunkel, M., Leinert, C., & Zinnecker, H. 2000, *A&A*, 356, 541
 Kastner, J. H., Huenemoerder, D. P., Schulz, N. S., Canizares, C. R., & Weintraub, D. A. 2002, *ApJ*, 567, 434
 Landolt, A. U. 1992, *AJ*, 104, 340
 Mamajek, E. E., Meyer, M. R., Hinz, P. M., et al. 2004, *ApJ*, 612, 496
 Martin, E. L. 1998, *AJ*, 115, 351
 Martín, E. L., Delfosse, X., & Guieu, S. 2004, *AJ*, 127, 449
 Mazzotta, P., Mazzitelli, G., Colafrancesco, S., & Vittorio, N. 1998, *A&AS*, 133, 403
 Mohanty, S., Jayawardhana, R., & Basri, G. 2004, *ApJ*, 609, 885
 Neuhaeuser, R., Sterzik, M. F., Schmitt, J. H. M. M., Wichmann, R., & Krautter, J. 1995, *A&A*, 297, 391
 Ozawa, H., Grosso, N., & Montmerle, T. 2005, *A&A*, 429, 963
 Pallavicini, R., Golub, L., Rosner, R., et al. 1981, *ApJ*, 248, 279
 Pillitteri, I., Micela, G., Damiani, F., & Sciortino, S. 2006, *A&A*, 450, 993
 Pizzolato, N., Maggio, A., Micela, G., Sciortino, S., & Ventura, P. 2003, *A&A*, 397, 147
 Pravdo, S. H., Feigelson, E. D., Garmire, G., et al. 2001, *Nature*, 413, 708
 Preibisch, T., Brown, A. G. A., Bridges, T., Guenther, E., & Zinnecker, H. 2002, *AJ*, 124, 404
 Preibisch, T., & Feigelson, E. D. 2005, *ApJS*, 160, 390
 Preibisch, T., & Zinnecker, H. 1999, *AJ*, 117, 2381
 Preibisch, T., Guenther, E., Zinnecker, H., et al. 1998, *A&A*, 333, 619
 Preibisch, T., Kim, Y.-C., Favata, F., et al. 2005, *ApJS*, 160, 401
 Reale, F., Betta, R., Peres, G., Serio, S., & McTiernan, J. 1997, *A&A*, 325, 782
 Reale, F., Güdel, M., Peres, G., & Audard, M. 2004, *A&A*, 416, 733
 Rosati, P., Borgani, S., & Norman, C. 2002, *ARA&A*, 40, 539
 Sciortino, S., Damiani, F., Favata, F., & Micela, G. 1998, *A&A*, 332, 825
 Siess, L., Dufour, E., & Forestini, M. 2000, *A&A*, 358, 593
 Slawson, R. W., Hill, R. J., & Landstreet, J. D. 1992, *ApJS*, 82, 117
 Slesnick, C. L., Carpenter, J. M., & Hillenbrand, L. A. 2006, *AJ*, 131, 3016
 Smith, R. K., Brickhouse, N. S., Liedahl, D. A., & Raymond, J. C. 2001, *ApJ*, 556, L91
 Stassun, K. G., Ardila, D. R., Barsony, M., Basri, G., & Mathieu, R. D. 2004, *AJ*, 127, 3537
 Stelzer, B., & Neuhaeuser, R. 2001, *A&A*, 377, 538
 Stelzer, B., Flaccomio, E., Montmerle, T., et al. 2005, *ApJS*, 160, 557
 Symington, N. H., Harries, T. J., Kurosawa, R., & Naylor, T. 2005, *MNRAS*, 358, 977
 Tsuboi, Y., Koyama, K., Murakami, H., et al. 1998, *ApJ*, 503, 894
 Tsujimoto, M., Koyama, K., Tsuboi, Y., Goto, M., & Kobayashi, N. 2002, *ApJ*, 566, 974
 Voges, W., Aschenbach, B., Boller, T., et al. 1999, *A&A*, 349, 389
 Walter, F. M., Vrba, F. J., Mathieu, R. D., Brown, A., & Myers, P. C. 1994, *AJ*, 107, 692
 White, R. J., & Basri, G. 2003, *ApJ*, 582, 1109

Online Material

Table 1. Log of the two *XMM* observations of Upper Scorpius star-forming region. Filtered exposures refer to screened time intervals, selected because not affected by high background count rates.

EPIC Instrument	Science mode	Optical blocking filter	Exposure (ks)		Observation start (UT)
			total	filtered	
Upper Scorpius – field 1 – rev. 130 – ObsId 0109060201 – RA = 16:14:00.0 Dec = –23:00:00.0					
PN	Full Frame	Medium	53.3	45.7	2000 Aug. 24 21:04:08
MOS1	Full Frame	Medium	53.3	50.0	2000 Aug. 24 20:23:08
MOS2	Full Frame	Medium	52.8	50.4	2000 Aug. 24 20:23:05
Upper Scorpius – field 2 – rev. 131 – ObsId 0112380101 – RA = 15:56:25.0 Dec = –23:37:47.0					
PN	Full Frame	Medium	42.7	36.3	2000 Aug. 26 23:41:37
MOS1	Full Frame	Medium	43.8	39.8	2000 Aug. 26 23:00:43
MOS2	Full Frame	Medium	43.8	40.0	2000 Aug. 26 23:00:37

Table 2. Photometric observations of Upper Scorpius selected fields: the field center, the size of the FOV, the instrument, and the broad band filters employed.

RA (J2000)	Dec (J2000)	FOV area	Instrument	Bands
15:56:20.8	–23:31:60	1°9′ × 1°9′	Curtis Schmidt	$UBVR_cI_c$
15:58:52.0	–22:49:47	"	"	"
15:56:21.5	–23:37:27	13′40″ × 13′40″	Danish 1.54m	VR_cI_c
15:56:21.4	–23:52:28	"	"	"
15:55:00.5	–24:00:52	"	"	"
15:55:00.5	–23:47:41	"	"	"
15:55:19.4	–23:17:04	"	"	"
15:54:09.4	–23:21:16	"	"	"
15:58:05.3	–23:06:53	"	"	"

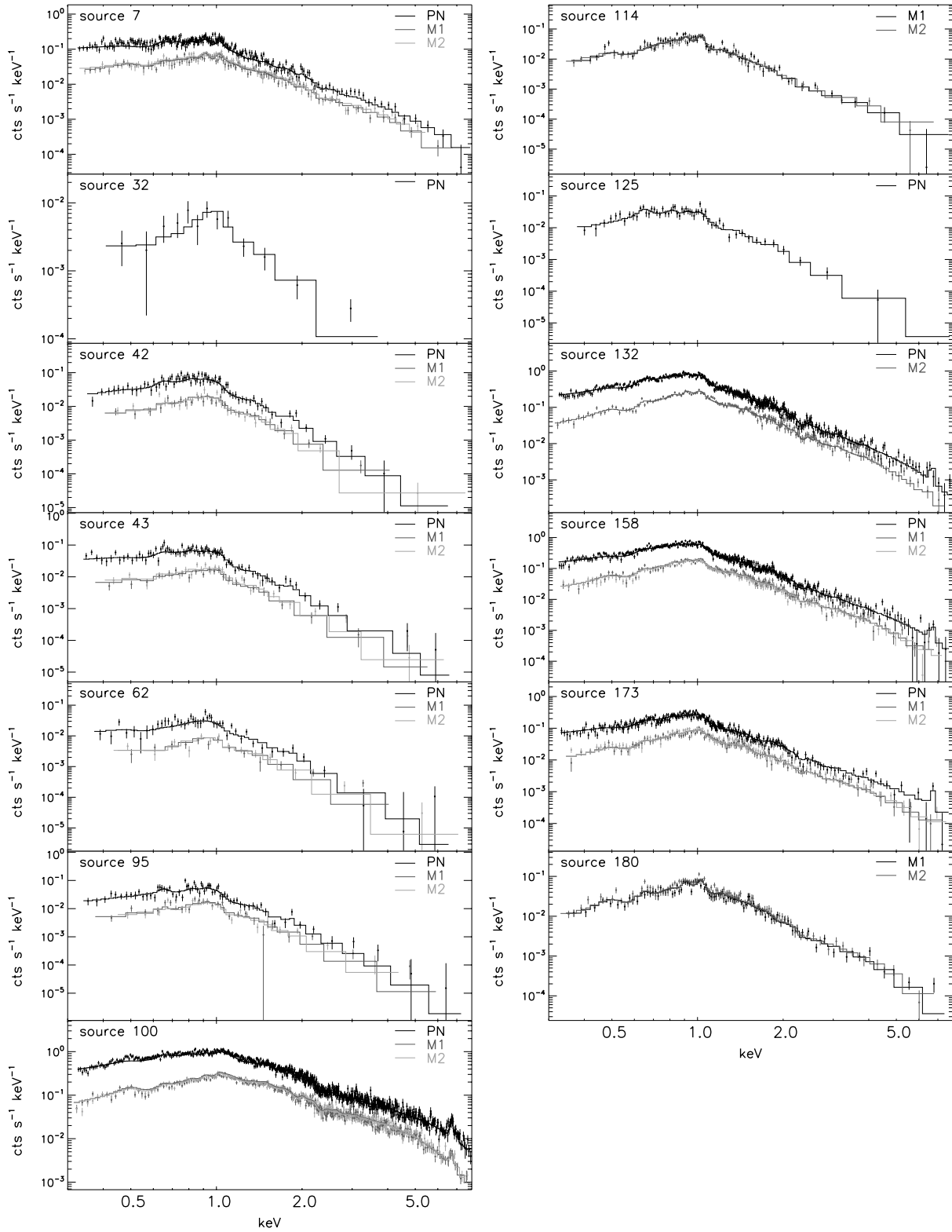


Fig. 6. EPIC spectra of the X-ray brightest USco members. Black indicates PN observed and predicted spectra, while dark gray and light gray mark the MOS1 and MOS2 spectra, respectively. The left column contains sources detected in the field 2 observation, while right column those of field 1.

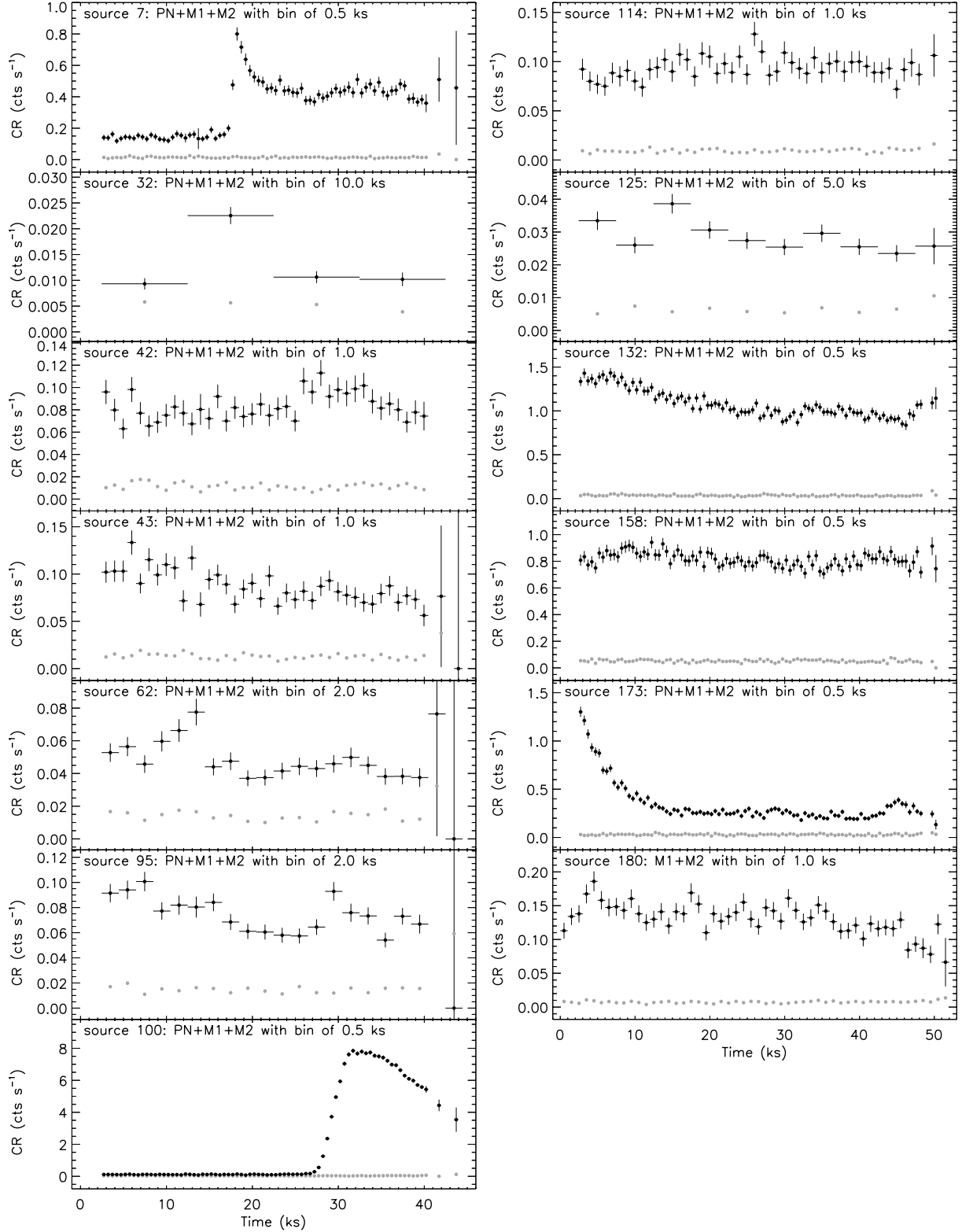


Fig. 7. Light curves of the USco members that turned out to be variable at the 99% confidence level by applying the KS test. Light curves are obtained by adding the counts of all the EPIC instruments. Light curves are not background-subtracted, background level is shown by gray dots, and it is constant in all cases. The origin on the abscissa correspond to the observation start time. Sources displayed in the left column are those of field 2, and the right column contains sources of field 1.

Appendix A: Results of the flare analysis**Table A.1.** Time-resolved analysis of the flare of source 7. Fits were performed with $N_{\text{H}} = 0.32 \times 10^{21} \text{ cm}^{-2}$. Unabsorbed X-ray luminosity is computed in the 0.5–8.0 keV band and takes the whole (flaring + quiescent) X-ray emission into account.

Int.	$T(\text{MK})$	$EM(10^{52} \text{ cm}^{-3})$	$\text{Fe}/\text{Fe}_{\odot}$	$\log L_{\text{X}}(\text{erg s}^{-1})$
q1	$8.5^{+0.7}_{-0.8}$	$15.8^{+3.0}_{-3.3}$	$0.10^{+0.05}_{-0.03}$	29.89
r1	≥ 8.6	$10.5^{+11.2}_{-10.5}$	$0.17^{+24.54}_{-0.17}$	30.19
d1	$27.2^{+12.4}_{-8.4}$	$37.6^{+14.1}_{-13.8}$	$1.01^{+2.30}_{-0.68}$	30.77
d2	$23.7^{+9.5}_{-5.0}$	$32.0^{+7.4}_{-8.4}$	$0.41^{+0.70}_{-0.27}$	30.60
d3	$21.8^{+6.0}_{-5.4}$	$29.1^{+6.1}_{-4.9}$	$0.16^{+0.22}_{-0.14}$	30.50
q2	$17.8^{+1.7}_{-1.7}$	$30.4^{+3.2}_{-3.1}$	$0.14^{+0.08}_{-0.06}$	30.47

Table A.2. Time-resolved analysis of the flare of source 100. Fits were performed with $N_{\text{H}} = 1.3 \times 10^{21} \text{ cm}^{-2}$. Unabsorbed X-ray luminosity is computed in the 0.5–8.0 keV band and takes the whole (flaring + quiescent) X-ray emission into account.

Int.	$T(\text{MK})$	$EM(10^{52} \text{ cm}^{-3})$	$\text{Fe}/\text{Fe}_{\odot}$	$\log L_{\text{X}}(\text{erg s}^{-1})$
q1	$8.6^{+1.0}_{-0.9}$	$18.8^{+3.7}_{-3.4}$	$0.02^{+0.02}_{-0.01}$	29.79
r1	$62.4^{+27.1}_{-12.6}$	$77.7^{+10.2}_{-9.8}$	$0.42^{+0.56}_{-0.42}$	31.08
r2	$68.6^{+12.7}_{-10.6}$	$338.0^{+27.0}_{-27.0}$	$0.43^{+0.36}_{-0.31}$	31.71
r3	$51.9^{+6.2}_{-6.1}$	$516.4^{+33.8}_{-33.6}$	$0.47^{+0.24}_{-0.22}$	31.86
p1	$38.8^{+4.7}_{-2.6}$	$654.9^{+36.3}_{-40.5}$	$0.32^{+0.16}_{-0.12}$	31.89
p2	$34.6^{+2.5}_{-2.5}$	$708.6^{+36.6}_{-36.3}$	$0.14^{+0.10}_{-0.09}$	31.87
d1	$33.1^{+2.1}_{-2.7}$	$686.2^{+28.0}_{-27.6}$	$0.17^{+0.08}_{-0.07}$	31.85
d2	$30.1^{+2.2}_{-1.7}$	$622.1^{+30.7}_{-30.3}$	$0.18^{+0.08}_{-0.07}$	31.79
d3	$29.7^{+1.5}_{-1.5}$	$539.8^{+22.6}_{-22.3}$	$0.13^{+0.06}_{-0.06}$	31.71
d4	$26.7^{+1.2}_{-3.5}$	$442.3^{+19.7}_{-16.6}$	$0.12^{+0.05}_{-0.05}$	31.60

Table A.3. Time-resolved analysis of the flare of source 132. Fits were performed with $N_{\text{H}} = 1.6 \times 10^{21} \text{ cm}^{-2}$. Unabsorbed X-ray luminosity is computed in the 0.5–8.0 keV band and takes the whole (flaring + quiescent) X-ray emission into account.

Int.	$T(\text{MK})$	$EM(10^{52} \text{ cm}^{-3})$	$\text{Fe}/\text{Fe}_{\odot}$	$\log L_{\text{X}}(\text{erg s}^{-1})$
p1	$34.3^{+6.2}_{-4.8}$	$29.5^{+2.7}_{-2.7}$	= 0.21	30.92
d1	$29.2^{+8.1}_{-5.0}$	$22.7^{+2.7}_{-2.9}$	= 0.21	30.87
d2	$8.7^{+2.7}_{-0.7}$	$14.1^{+2.4}_{-2.4}$	= 0.21	30.80
d3	$8.0^{+1.5}_{-0.6}$	$7.7^{+1.9}_{-1.9}$	= 0.21	30.76
d4	$7.8^{+1.7}_{-4.4}$	$3.8^{+2.1}_{-1.9}$	= 0.21	30.74
r1	$7.9^{+1.9}_{-3.6}$	$3.6^{+2.3}_{-3.6}$	= 0.21	30.74
d5	$7.9^{+0.9}_{-2.1}$	$4.7^{+2.0}_{-1.8}$	= 0.21	30.75
q1	$3.7^{+0.7}_{-0.5}, 13.7^{+10.8}_{-10.4}$	$35.7^{+7.0}_{-7.2}, 51.4^{+4.3}_{-4.2}$	= 0.21	30.72
r2	$7.9^{+1.9}_{-3.4}$	$5.4^{+3.3}_{-5.4}$	= 0.21	30.75

Table A.4. Time-resolved analysis of the flare of source 173. Fits were performed with $N_{\text{H}} = 1.2 \times 10^{21} \text{ cm}^{-2}$. Unabsorbed X-ray luminosity is computed in the 0.5–8.0 keV band and takes the whole (flaring + quiescent) X-ray emission into account.

Int.	$T(\text{MK})$	$EM(10^{52} \text{ cm}^{-3})$	$\text{Fe}/\text{Fe}_{\odot}$	$\log L_{\text{X}}(\text{erg s}^{-1})$
p1	$22.5^{+3.2}_{-4.0}$	$75.5^{+5.4}_{-5.4}$	= 0.35	30.90
d1	$21.6^{+2.3}_{-2.2}$	$47.5^{+2.9}_{-2.9}$	= 0.35	30.72
d2	$18.0^{+1.5}_{-1.2}$	$28.6^{+2.0}_{-1.9}$	= 0.35	30.54
d3	$14.2^{+0.8}_{-1.3}$	$7.4^{+0.6}_{-0.8}$	= 0.35	30.19
q1	$8.7^{+0.6}_{-1.2}, 18.6^{+16.8}_{-11.2}$	$5.0^{+0.8}_{-1.4}, 3.9^{+1.0}_{-1.0}$	= 0.35	29.94
r1	$159.7^{+400.8}_{-107.7}$	$3.0^{+0.5}_{-0.6}$	= 0.35	30.13
d4	$27.4^{+51.4}_{-12.0}$	$3.3^{+1.1}_{-1.1}$	= 0.35	30.08